A TWO-PARAMETER CRITERION FOR CLASSIFYING THE EXPLODABILITY OF MASSIVE STARS BY THE NEUTRINO-DRIVEN MECHANISM

T. Ertl[1,2], H.-Th. Janka[1], S. E. Woosley[3], T. Sukhbold[3], and M. Ugliano[4]

Draft version January 16, 2022

ABSTRACT

Thus far, judging the fate of a massive star (either a neutron star (NS) or a black hole) solely by its structure prior to core collapse has been ambiguous. Our work and previous attempts find a non-monotonic variation of successful and failed supernovae with zero-age main-sequence mass, for which no single structural parameter can serve as a good predictive measure. However, we identify two parameters computed from the pre-collapse structure of the progenitor, which in combination allow for a clear separation of exploding and non-exploding cases with only few exceptions ($\sim$1–2.5%) in our set of 621 investigated stellar models. One parameter is M_4, defining the normalized enclosed mass for a dimensionless entropy per nucleon of $s = 4$, and the other is $\mu_4 \equiv (\mathrm{d}m/M_\odot)/(\mathrm{d}r/1000\,\mathrm{km})|_{s=4}$, being the normalized mass-derivative at this location. The two parameters μ_4 and $M_4\mu_4$ can be directly linked to the mass-infall rate, $\dot{M}$, of the collapsing star and the electron-type neutrino luminosity of the accreting proto-NS, $L_{\nu_e} \propto M_{\mathrm{ns}}\dot{M}$, which play a crucial role in the "critical luminosity" concept for the theoretical description of neutrino-driven explosions as runaway phenomenon of the stalled accretion shock. All models were evolved employing the approach of Ugliano et al. for simulating neutrino-driven explosions in spherical symmetry. The neutrino emission of the accretion layer is approximated by a gray transport solver, while the uncertain neutrino emission of the 1.1 $M_\odot$ proto-NS core is parametrized by an analytic model. The free parameters connected to the core-boundary prescription are calibrated to reproduce the observables of Supernova 1987A for five different progenitor models.

Subject headings: supernovae: general — stars: massive — hydrodynamics — neutrinos

1. INTRODUCTION

Presupernova stars in the mass range above $\sim$9 $M_\odot$ exhibit large variations of their structure with respect to, e.g., their Fe-core and O-core masses, their binding energies, and their density or entropy profiles above the Fe-core (Woosley et al. 2002). These properties vary non-monotonically with the zero-age main-sequence (ZAMS) mass and can differ considerably even between progenitors with only a small difference of their ZAMS masses (Sukhbold & Woosley 2014).

Correspondingly, Ugliano et al. (2012) found that the properties of neutrino-driven supernovae (SNe) like explosion energy, nickel mass, and remnant mass change non-monotonically with the ZAMS mass. In particular, for the investigated grid of 101 solar-metallicity progenitors binned in 0.2 $M_\odot$ steps (Woosley et al. 2002), they found islands of non-exploding, black hole (BH) forming cases down to 15 $M_\odot$, alternating with mass-intervals of exploding progenitors. In a few cases individual neighboring progenitors showed opposite behavior.

Ugliano et al. (2012) used a simple, parametric model for the contracting proto-neutron star (PNS) as a neutrino source to trigger neutrino-driven explosions in spherically symmetric (1D) hydrodynamic simulations, but their basic findings were confirmed by other groups working with semi-analytic descriptions in 1D (Pejcha & Thompson 2015) and approximate neutrino transport in two- and three-dimensional (2D,

tertl@mpa-garching.mpg.de, thj@mpa-garching.mpg.de

[1] Max-Planck-Institut für Astrophysik, Karl-Schwarzschild-Str. 1, 85748 Garching, Germany

[2] Physik Department, Technische Universität München, James-Franck-Straße 1, 85748 Garching, Germany

[3] Department of Astronomy and Astrophysics, University of California, Santa Cruz, CA 95064

[4] Institut für Kernphysik, Technische Universität Darmstadt, Schlossgartenstr. 2, 64289 Darmstadt, Germany

3D) hydrodynamic models (Nakamura et al. 2015; Horiuchi et al. 2014). While O'Connor & Ott (2011) suggested that BH formation requires a compactness (normalized enclosed mass-radius ratio) of $\xi_{2.5} > 0.45$ with

$$\xi_M \equiv \frac{M/M_\odot}{R(M)/1000\,\mathrm{km}}, \quad (1)$$

Ugliano et al. (2012) obtained only explosions for $\xi_{2.5} < 0.15$, explosions or BH formation for $0.15 \leq \xi_{2.5} \leq 0.35$, and only BH formation for $\xi_{2.5} > 0.35$, which implies a larger fraction of BH formation cases for solar-metallicity stars. Horiuchi et al. (2014) pointed out that a critical compactness of $\xi_{2.5} \gtrsim 0.2$ for failed explosions is compatible with a lack of red supergiant Type-IIP SN progenitors above $\sim$16 $M_\odot$ (Smartt et al. 2009) and with a significant excess of the star-formation rate compared to the observed SN rate (Horiuchi et al. 2011). Pejcha & Thompson (2015) showed that their parameterization "case (a)", which yields results similar to those of Ugliano et al. (2012), is close to being optimally compatible with a combination of several observational constraints.

How can the non-monotonicities of the explodability be understood in terms of the pre-supernova properties and in the context of the physics of the neutrino-driven mechanism? Are there characteristic parameters of the pre-supernova star that decide better about success or failure of the explosion than a single value of the compactness or other, similarly useful parameters like the iron-core mass or the binding energy outside of the iron core? While all these measures reflect trends like an enhanced tendency of BH formation for high compactness, large iron-core mass or high exterior binding energy, there are still many outliers that do not obey the correlations. For example, a suitably chosen mass M of the compactness ξ_M allows to correctly predict explosions in <90% of the cases (Pejcha & Thompson 2015), but the best choice of M is merely empir-

ical and the physical justification of ξ_M as a good diagnostics is unclear.

Here we propose a two-parameter criterion that separates successful explosions from failures with very high reliability. While two compactness values, e.g. $\xi_{1.5}$ and $\xi_{2.5}$, or the iron-core mass and the mean entropy in some suitable mass range begin to show such a disentanglement, we demonstrate that the normalized mass inside a dimensionless entropy per nucleon of $s = 4$,

$$M_4 \equiv m(s = 4)/M_\odot, \qquad (2)$$

and the mass derivative at this location,

$$\mu_4 \equiv \left. \frac{\mathrm{d}m/M_\odot}{\mathrm{d}r/1000\,\mathrm{km}} \right|_{s=4}, \qquad (3)$$

both determined from the pre-supernova profiles, allow to predict the explosion behavior successfully in $\gtrsim 97\%$ of all cases and have a direct connection with the theoretical basis of the neutrino-driven mechanism.

We briefly describe our numerical approach in Sect. 2, including a detailed discussion of our modeling methodology in comparison to other approaches in the recent literature, present our results in Sect. 3, and conclude in Sect. 4.

2. NUMERICAL SETUP AND PROGENITOR MODELS

2.1. Modeling approach

Our basic modeling approach follows Ugliano et al. (2012) with a number of improvements. To trigger neutrino-driven explosions in spherically symmetric (1D) hydrodynamic simulations, we use a schematic model of the high-density core of the PNS as neutrino source (for details, see Ugliano et al. 2012). This analytic description is applied to the innermost $1.1\,M_\odot$, which are excised from the computational domain, and it yields time-dependent neutrino luminosities that are imposed as boundary values at the contracting, Lagrangian inner grid boundary. On the numerical grid, where neutrino optical depths increase from initially ~ 10 to finally several 1000, neutrino transport is approximated by the gray treatment described in Scheck et al. (2006) and Arcones et al. (2007). This allows us to account for the progenitor-dependent variations of the accretion luminosity.

Our approach replaces still uncertain physics connected to the equation of state (EoS) and neutrino opacities at high densities by a simple, computationally efficient PNS core model. The associated free parameters are calibrated by reproducing observational properties of SN 1987A. We emphasize that the neutrino emission is sensitive to the time and progenitor dependent mass accretion rate. Not only the accretion luminosity increases for progenitors with higher mass accretion rate of the PNS, but also the neutrino loss of the inner core rises with the accreted mass because of compressional work of the accretion layer on the core. Such dependences are accounted for in our modeling of NS core and accretion.

Our numerical realization improves the treatment by Ugliano et al. (2012) in several aspects. We use the high-density EoS of Lattimer & Swesty (1991) with a compressibility of $K = 220\,\mathrm{MeV}$ and below $\rho = 10^{11}\,\mathrm{g\,cm^{-3}}$ apply an $e^\pm$, photon, and baryon EoS (Timmes & Swesty 2000) for nuclear statistical equilibrium (NSE; Kifonidis 2004, private communication) with 16 nuclei for $T > 7 \times 10^9$ K and a 14-species alpha network (including an additional neutron-rich tracer nucleus of iron-group material) at lower temperatures (Müller 1986). The tracer nucleus is assumed to be formed
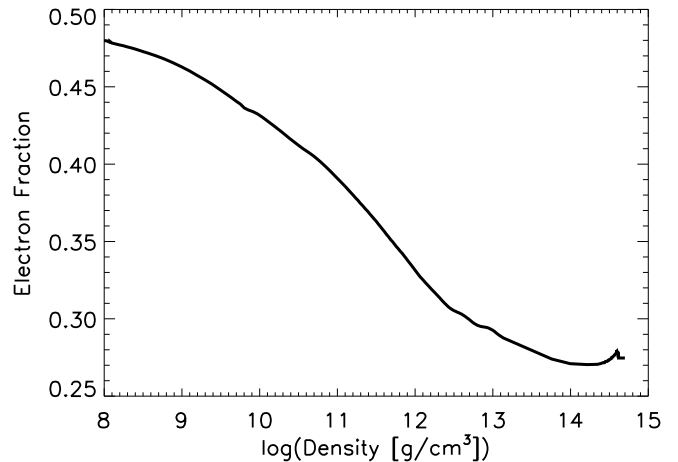

Fig. 1.— Electron fraction as function of density, $Y_e(\rho)$, for modeling the deleptonization of the collapsing stellar iron core during the infall phase until core bounce according to the approximate treatment of Liebendörfer (2005).

in ejecta with $Y_e < 0.49$ and thus tracks the ejection of matter with neutron excess, when detailed nucleosynthesis calculations predict little production of ^{56}Ni (Thielemann et al. 1996).

The network is consistently coupled to the hydrodynamic modeling and allows us to include the contribution from explosive nuclear burning to the energetics of the SN explosions. The collapse phase until core bounce is modeled with the deleptonization scheme proposed by Liebendörfer (2005), using the $Y_e(\rho)$ trajectory of Fig. 1 for the evolution of the electron fraction Y_e as function of density ρ (Müller 2013, private communication). This yields good overall agreement with full neutrino transport results and allows for a very efficient computation of large sets of post-bounce models.

2.2. Progenitor models

We perform collapse and explosion simulations for large progenitor sets of different metallicities, namely: the zero-metallicity z2002 set (30 models with ZAMS masses of 11.0–40.0 $M_\odot$), low-metallicity (10^{-4} solar) u2002 series (247 models, 11.0–75.0 $M_\odot$), and the solar-metallicity s2002 series (101 models, 10.8–75.0 $M_\odot$) of Woosley et al. (2002) plus a 10.0 $M_\odot$ progenitor (Woosley 2007, private communication) and a 10.2 $M_\odot$ progenitor (Heger 2003, private communication); the solar-metallicity s2014 (151 models, 15.0–30.0 $M_\odot$) and sh2014 series (15 models, 30.0–60.0 $M_\odot$, no mass loss) of Sukhbold & Woosley (2014), supplemented by additional 36 models with 9.0–14.9 $M_\odot$; the solar-metallicity s2007 series (32 models, 12.0–120.0 $M_\odot$) of Woosley et al. (2007); and the n2006 series (8 models, 13.0–50.0 $M_\odot$; Nomoto et al. 2006).

For the core-model parameter calibration we choose five different progenitors, namely the (red supergiant) model s19.8 of the s2002 series as in Ugliano et al. (2012), and four blue supergiant pre-supernova models of SN 1987A: w15.0 (ZAMS mass of 15 $M_\odot$; Woosley et al. 1988), w18.0 (18 $M_\odot$, evolved with rotation; Woosley et al. 2007), w20.0 (20 $M_\odot$; Woosley et al. 1997), and n20.0 (20 $M_\odot$; Shigeyama & Nomoto 1990). Compactness values and explosion and remnant parameters of these models are listed in Table 1.

The calibration aims at producing the explosion energy and ejected ^{56}Ni mass of SN 1987A compatible with observations, for which the best values are $E_{\mathrm{exp}} = (1.50 \pm 0.12) \times 10^{51}$ erg (Utrobin 2005), $E_{\mathrm{exp}} \sim 1.3 \times 10^{51}$ erg (Utrobin & Chugai

TABLE 1
CALIBRATION MODELS WITH EXPLOSION AND REMNANT PROPERTIES

Calibration Model	$\xi_{1.5}$[a]	$\xi_{1.75}$[a]	$\xi_{2.0}$[a]	$\xi_{2.5}$[a]	$t_{\rm exp}$[b] [ms]	$E_{\rm exp}$[c] [B]	$M_{\rm ej}$[d] [$M_\odot$]	$E_{\rm exp}/M_{\rm ej}$ [B/$M_\odot$]	$M_{^{56}{\rm Ni}}$[e] [$M_\odot$]	$M_{\rm tracer}$[f] [$M_\odot$]	$M_{\rm ns}$[g] [$M_\odot$]	$M_{\rm wind}$[h] [$M_\odot$]	$M_{\rm fb}$[i] [$M_\odot$]	$t_{\nu,90}$[j] [s]	$E_{\nu,{\rm tot}}$[k] [100 B]
s19.8 (2002)	1.03	0.35	0.22	0.14	750	1.30	12.98	0.100	0.072	0.034	1.55	0.096	0.00298	4.27	3.68
w15.0	0.34	0.09	0.03	0.01	580	1.41	13.70	0.103	0.045	0.046	1.32	0.088	0.00018	5.18	2.81
w18.0	0.76	0.26	0.16	0.10	730	1.25	15.42	0.081	0.056	0.036	1.48	0.081	0.00310	4.16	3.32
w20.0	0.98	0.35	0.18	0.06	620	1.24	17.81	0.070	0.063	0.027	1.56	0.089	0.00168	4.73	3.61
n20.0	0.87	0.36	0.19	0.12	560	1.49	14.84	0.100	0.036	0.052	1.55	0.117	0.00243	3.97	3.48

[a] Compactness evaluated for a central density of $5 \times 10^{10}\,{\rm g\,cm^{-3}}$. For w15.0 the value at core bounce is given because earlier data are not available.

[b] Post-bounce time of onset of explosion, when shock expands beyond 500 km (1 B = 1 bethe = 10^{51} erg).

[c] Final explosion energy, including binding energy of preshock progenitor.

[d] Mass ejected in the explosion.

[e] Ejected ^{56}Ni mass produced by explosive burning with late-time fallback taken into account.

[f] Mass of neutron-rich tracer nucleus ejected in neutrino-driven wind material with neutron excess (fallback is taken into account).

[g] Final baryonic neutron-star mass including late-time fallback.

[h] Neutrino-driven wind mass measured by mass between gain radius at $t_{\rm exp}$ and preliminary mass cut *before* fallback.

[j] Fallback mass.

[j] Emission time for 90% of the radiated neutrino energy.

[k] Total radiated neutrino energy.

2011), and $M_{\rm Ni} = 0.0723$–$0.0772\,M_\odot$ (Utrobin et al. 2014), but numbers reported by other authors cover a considerable range (cf. Handy et al. 2014 for a compilation). The explosion energy that we accept for a SN1987A model in the calibration process is guided by the ejected ^{56}Ni mass (which fully accounts for short-time and long-time fallback) and a ratio of $E_{\rm exp}$ to ejecta mass in the ballpark of estimates based on light-curve analyses (cf. Table 1 for our values).

Because of the "gentle" acceleration of the SN shock by the neutrino-driven mechanism (also in 3D simulations, see Utrobin et al. 2014), it is difficult to produce this amount of ejected ^{56}Ni just by shock-induced explosive burning. $M_{^{56}{\rm Ni}}$ in Table 1 mainly measures this component but also contains ^{56}Ni from proton-rich neutrino-processed ejecta. However, also neutrino-processed ejecta and the neutrino-driven wind with a slight neutron excess could contribute significantly to the ^{56}Ni production. The electron fraction Y_e of these ejecta is set by ν_e and $\bar\nu_e$ interactions and depends extremely sensitively on the properties (luminosities and spectra) of the emitted neutrinos, which our transport approximation cannot reliably predict and which also depend on subtle effects connected to multi-dimensional physics and neutrino opacities. For these reasons we consider the ^{56}Ni as uncertain within the limits set by the true ^{56}Ni yield from our network on the low side and, in the maximal case, all tracer material added to that. We therefore provide as possible ^{56}Ni production of our models the range $M_{^{56}{\rm Ni}} \leq M_{^{56}{\rm Ni}}^{\rm total} \leq M_{^{56}{\rm Ni}} + M_{\rm tracer}$.

Different from Ugliano et al. (2012) we reduce the compression parameter of the NS core model by a linear relation $\zeta' \propto \xi_{1.75,\rm b}$ (the value of $\xi_{1.75,\rm b}$ is measured at core bounce) for progenitors with $\leq 13.5\,M_\odot$, i.e., we use the function

$$\zeta' = \zeta \left(\frac{\xi_{1.75,\rm b}}{0.5} \right) \quad {\rm for} \ \ M \leq 13.5\,M_\odot, \qquad (4)$$

with ζ being the value determined from the SN 1987A calibration for a considered progenitor model of that supernova. We note that the values of $\xi_{1.75,\rm b}$ are less than 0.5 for all progenitors below $13.5\,M_\odot$ and close to 0.5 for $M \sim 13.5\,M_\odot$, for which reason Eq. (4) connects smoothly to the ζ value applied for stars above $13.5\,M_\odot$ according to the SN 1987A calibration.

The modification of Eq. (4) accounts for the reduced bur-

den of the small mass of the accretion layer of these stars with their extremely low compactnesses. Such a modification allows us to reproduce the trend to weak explosions obtained in sophisticated 2D and 3D simulations for low-mass iron-core progenitors (Janka et al. 2012; Melson et al. 2015a; Müller 2015). We point out that the Crab supernova SN 1054 is considered to be connected to the explosion of a $\sim 10\,M_\odot$ star (e.g., Nomoto et al. 1982; Smith 2013), and its explosion energy is estimated to be up to only $\sim 10^{50}$ erg (e.g., Yang & Chevalier 2015). This fact lends support to the results of recent, self-consistent 1D and multi-dimensional supernova models of $\lesssim 10\,M_\odot$ stars (e.g., Kitaura et al. 2006; Fischer et al. 2010; Melson et al. 2015a), whose low explosion energies and low nickel production agree with the Crab observations.

Although as a consequence of our ζ reduction the explosion times, $t_{\rm exp}$, tend to be late for stars in the 10.5–$12.5\,M_\odot$ range (Fig. 3), this behavior also seems to be compatible with self-consistent, multi-dimensional simulations of stellar explosions in the 11–$12\,M_\odot$ range by Müller et al. (2013), Müller (2015), and Janka et al. (2012), where these stars were found to have a long-lasting phase of accretion and simultaneous mass outflow after a quite inert onset of the explosion. A more detailed discussion and justification of our modified treatment of low-ZAMS mass cases will be provided in Sect. 2.3.4 and can also be found in a follow-up paper by Sukhbold et al. (2015), where the values of all PNS core-model parameters are tabulated for all calibrations.

It must be emphasized that in the context of the present work the detailed treatment of the low-mass stars is not overly important. These stars usually explode fairly easily, independent of the treatment of the PNS core model with the original or with our revised calibration. Therefore these stars lie far away from the boundary curve that separates exploding from non-exploding models and whose determination will be our main goal in Sect. 3. For this reason exactly the same separation line is obtained when the core-model parameter values from the SN 1987A calibration are applied to all stars.

In Table 1 and the rest of our paper, time-dependent structural parameters of the stars (like compactness values, μ_4 of Eq. 3, the iron-core mass $M_{\rm Fe}$) are measured when the stars possess a central density of $5 \times 10^{10}\,{\rm g\,cm^{-3}}$, unless otherwise stated. This choice of reference density defines a clear standard for the comparison of stellar profiles of different progen-

itors (cf. Appendix A of Buras et al. 2006). Different from the moment of core bounce, which was used in other works, our reference density has the advantage to be still close to the initial state of the pre-collapse models provided by stellar evolution modeling and therefore to yield values of the structural parameters that are more similar to those of the pre-collapse progenitor data. Our calibration model w15.0, however, must be treated as an exception. Because pre-collapse profiles of this model are not available any more, all structural quantities for this case are given (roughly) at core bounce.

2.3. *Methodology and theory of neutrino-driven explosions*

2.3.1. *Status of "ab initio" supernova modeling*

"Ab initio", fully self-consistent simulations of stellar core collapse with state-of-the-art treatment of microphysics and neutrino transport do not lead to explosions in spherical symmetry except for stars with O-Ne-Mg and Fe-cores near the low-mass end of SN progenitors (Kitaura et al. 2006; Janka et al. 2008, 2012; Fischer et al. 2010; Melson et al. 2015a). 2D simulations in the recent past have produced successful explosions and underline the fundamental importance of multidimensional effects, but the true meaning of these results with respect to the neutrino-driven mechanism is not finally clear and the current situation is diffuse and contradictive.

On the one hand, some of the 2D explosions set in relatively late and might remain on the weak side (e.g., Marek & Janka 2009; Suwa 2012; Suwa et al. 2014; Müller et al. 2012a,b, 2013; Müller & Janka 2014; Müller 2015; Hanke 2014), although such apprehension is speculative because not all simulations could be continued until the explosion energy had saturated (Müller 2015). On the other hand, the Oak Ridge group obtained explosions much earlier after bounce with shock evolutions being astonishingly similar for 12, 15, 20, and 25 $M_\odot$ stars and explosion energies fairly compatible with observations (Bruenn et al. 2013, 2014). In contrast, Dolence et al. (2015) did not find any successes in 2D simulations of the same progenitors but they used a different treatment of gravity, hydrodynamics, equation of state, neutrino transport, and neutrino opacities. The exact reasons for the different findings will have to be clarified by detailed tests and comparisons. The situation is even more diffuse because current 3D simulations agree in showing slower explosions compared to 2D calculations or even no explosions (e.g., Hanke et al. 2012, 2013; Tamborra et al. 2014; Mezzacappa et al. 2015; Couch 2013; Couch & O'Connor 2014; Takiwaki et al. 2014) although some studies have proclaimed the opposite behavior (Nordhaus et al. 2010; Burrows 2013; Dolence et al. 2013). So far only a few recent 3D calculations with highly refined neutrino treatment have obtained successful shock revival by the neutrino-driven mechanism (Melson et al. 2015a,b; Lentz et al. 2015). Interestingly, the 3D simulation of a low-mass (9.6 $M_\odot$) progenitor with detailed neutrino physics, whose explosion energy approached its saturation level, was found to explode more energetically in 3D than in 2D (Melson et al. 2015a). This result is in line with a 2D-3D comparison in the 11–12 $M_\odot$ range conducted by Müller (2015). In both studies accretion downflows and the re-ejection of neutrino-heated matter were observed to be different in 2D and 3D because of geometry dependent differences of the Kelvin-Helmholtz instability and flow fragmentation. The 3D models therefore suggest that explosions in 2D are massively affected by the assumption of rotational symmetry around the polar grid axis and by an inverse turbulent energy cascade, which tends to amplify energy on the largest possible scales (Hanke et al. 2012) and also produces numerical artifacts in the post-explosion accretion phase of the neutron star (Müller 2015). It must therefore be suspected that the early onset of explosions and the extremely unipolar or bipolar deformations along the symmetry axis obtained in many 2D models could be artifacts of the imposed symmetry constraints.

2.3.2. *Modeling recipes in recent literature*

Before 3D modeling will have become a routine task and results will have converged, neutrino-driven explosions of large sets of progenitor stars can be explored for their observational implications only by referring to simplified modeling approaches. Several different recipes have been introduced for this recently. Ugliano et al. (2012) used an analytic PNS core-cooling model in connection with a neutrino transport approximation in 1D hydrodynamic explosion simulations (as briefly summarized in Sect. 2), thus improving the simpler, time-dependent boundary neutrino luminosity prescribed by previous users of the simulation code (Kifonidis et al. 2006; Scheck et al. 2004, 2006, 2008; Arcones et al. 2007; Arcones & Janka 2011) and the even simpler neutrino light-bulb treatment (without any transport approximation) applied by Janka & Müller (1996) and Kifonidis et al. (2003). O'Connor & Ott (2011) resorted to a scaling parameter f_{heat} to artificially enhance the neutrino heating by charged-current processes behind the stalled shock in 1D hydrodynamic models with approximate neutrino treatment. Nakamura et al. (2015) performed an extensive set of 2D simulations with simplified neutrino transport despite the grains of salt mentioned in Sect. 2.3.1 (see also Horiuchi et al. 2014, for cautioning against the 2D results). Pejcha & Thompson (2015) applied a semi-analytic model to determine the onset times of the explosions, using neutrino luminosities from 1D calculations of accreting PNSs, and estimated explosion properties by analytic arguments. Suwa et al. (2014) also performed 2D simulations and suggested analytic approximations for describing diffusion and accretion components of the neutrino luminosities from PNSs and a free-fall treatment for the collapse of the overlying stellar layers. Perego et al. (2015) invented a method they named "PUSH", which they applied to trigger explosions artificially in their general relativistic, 1D hydrodynamic core-collapse and PNS formation modeling with sophisticated neutrino transport. PUSH gradually switches on and off additional neutrino heating of chosen strength during a chosen period of time. This procedure is assumed to mimic the effects of multi-D hydrodynamics in the postshock region. The extra heating is coupled to the *heavy-lepton neutrino* emission from the PNS.

All of these recipes contain larger sets of parameters and degrees of freedom, which are either varied in exploring different cases (e.g., Pejcha & Thompson 2015) or are adjusted by comparison to more complete models (e.g., Suwa et al. 2014) or by reproducing observational benchmarks like those set by SN 1987A (Ugliano et al. 2012; Perego et al. 2015). The models of Ugliano et al. (2012) and those in the present paper assume that the explosion trigger is tightly coupled to the physics that reflects the main differences between different progenitor stars, namely to the post-bounce accretion history of the collapsing stellar core and the corresponding accretion luminosities of ν_e and $\bar{\nu}_e$. It will have to be seen whether this important aspect of the models remains being supported by future developments towards a more complete understanding of the physics of the central engine that powers the explosion
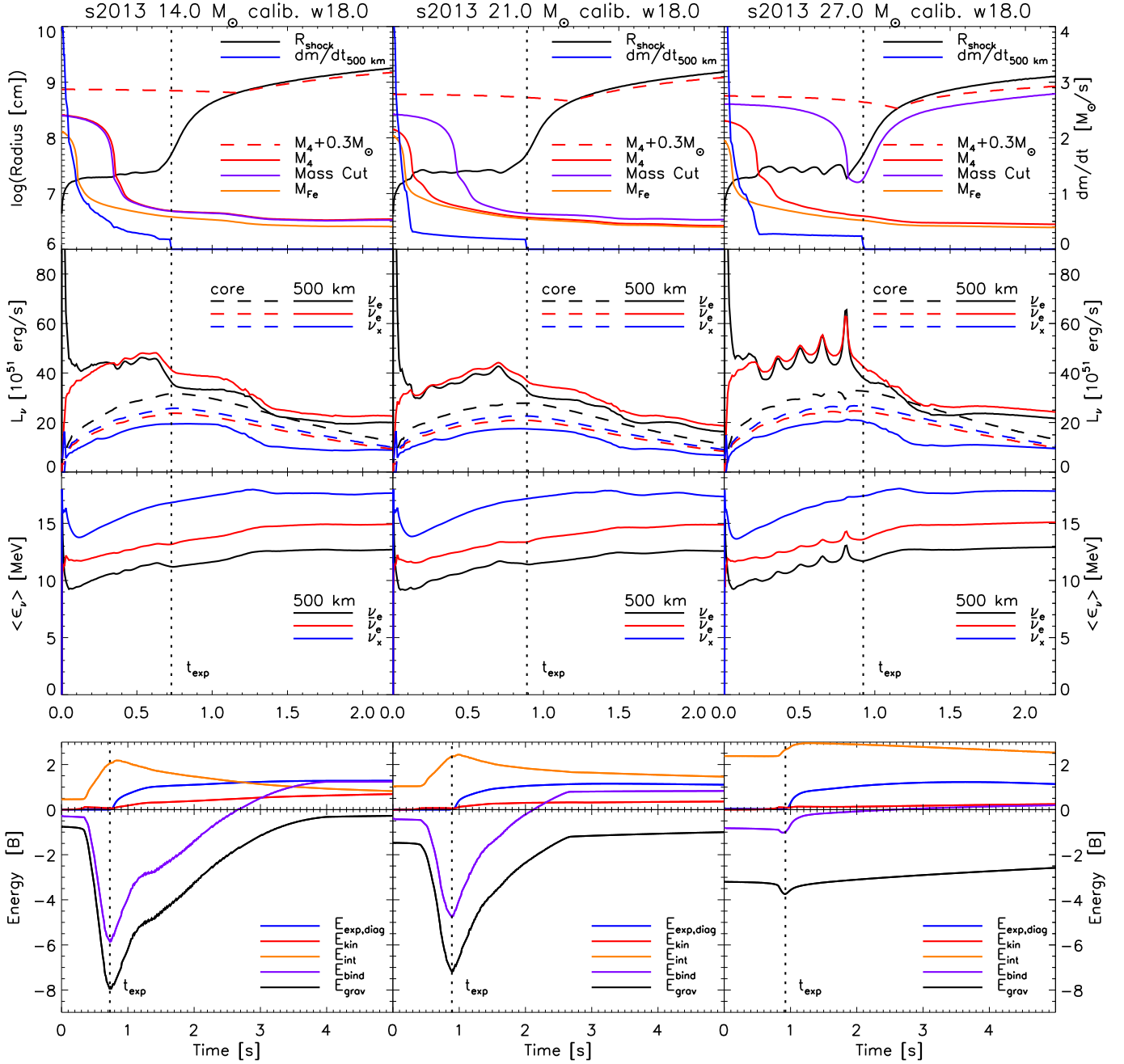
FIG. 2.— Models s14.0 (*left*), s21.0 (*middle*), and s27.0 (*right*) of the s2014 progenitor series as exemplary cases of successful explosions with the w18.0 calibration. The *top panels* display as functions of post-bounce time the radius of the outgoing shock (black line), the mass accretion rate measured at 500 km (blue line; scale on the right side), and the radii of iron core (orange), $M_4 = m(s = 4)$ (red), $M_4 + 0.3$ (red dashed) and trajectory of the final mass cut (after completion of fallback; purple). The *second panels from top* show the time evolution of the luminosities of ν_e, $\bar{\nu}_e$ and a single species of heavy-lepton neutrinos ν_x as labelled in the plot, measured at 500 km (solid lines) and at the inner grid boundary (dashed lines). The *third panels from top* show the mean energies of all neutrino kinds as radiated at 500 km. The vertical dotted lines indicate the onset time of the explosion as the moment when the outgoing shock passes the radius of 500 km. The *bottom panels* provide the time evolution of the diagnostic energy of the explosion (integrated energy of all postshock zones with positive total energy; blue line). Also shown are the kinetic energy (red), gravitational energy (black), and internal energy (orange) as integrals over the whole, final SN ejecta between the final mass cut (after fallback) on the one side and the stellar surface on the other. The total (binding) energy (purple) as the sum of these energies ultimately converges to the diagnostic energy and both of these energies asymptote to the final explosion energy. While this convergence is essentially reached after ~4 s in the case of s14.0, the expansion of shocked matter in the s21.0 model and thus the energy evolution is slowed down at ~2.7 s by the high densities in the stellar core. The s27.0 model becomes gravitationally unbound (i.e., the total binding energy becomes positive) even more slowly because of the very massive stellar core. The convergence of total energy and diagnostic energy takes tens of seconds in this case.

in the context of the neutrino-driven mechanism.

2.3.3. *Motivation of modeling assumptions of this work*

The analytic NS-core model introduced by Ugliano et al. (2012) in combination with their approximate transport solver for treating the accretion component of the neutrino luminosity as well as neutrino cooling and heating between PNS and shock, is an attempt to realize the tight coupling of accretion behavior and explodability in close similarity to what is found in current 2D simulations (e.g. those of Marek & Janka 2009; Müller et al. 2012a,b, 2013; Müller & Janka 2014). Since 1D models with elaborate neutrino physics and a fully self-consistent calculation of PNS cooling miss the critical condition for explosions by far, it is *not the goal* of Ugliano et al. (2012) to closely reproduce the neutrino emission properties of such more sophisticated calculations. Rather than that it is the goal to approximate the *combined effects of neutrino heating and multi-dimensional postshock hydrodynamics* by a simple and computationally efficient neutrino source model, which allows for the fast processing of large progenitor sets including the long-time evolution of the SN explosion to determine also the shock breakout and fallback evolution.

Free parameters in the NS core model and the prescribed contraction behavior of the inner grid boundary are calibrated by matching basic observational features (explosion energy, ^{56}Ni yield, total release of neutrino energy) of SN 1987A. This is intended to ensure that the overall properties of the neutrino-source model are anchored on empirical ground. Of course, the setting of the parameter values cannot be unambiguous when only a few elements of a single observed SN are used for deriving constraints. However, the approximate nature of the neutrino source treatment as a whole does not require the perfectly accurate description of each individual model component in order to still contain the essence of the physics of the system like important feedback effects between accretion and outflows and neutrinos, which govern the progenitor-dependent variations of explodability and SN properties. A reasonable interplay of the different components is more relevant than a most sophisticated representation of any single aspect of the neutrino source model.

In detail, the basic features of our 1D realization of the neutrino-driven mechanism along the lines of Ugliano et al. (2012) are the following:

- The possibility of an explosion is coupled closely to the progenitor-dependent strength and evolution of the post-bounce accretion. This is achieved not only by taking into account the accretion luminosity through the approximate neutrino transport scheme but also through the response of the PNS-core to the presence of a hot accretion mantle. The evolution of the latter is explicitly followed in our hydrodynamic simulations, which track the accumulation of the collapsing stellar matter around the inner PNS core. The existence of the mantle layer enters the analytic core model in terms of the parameter m_{acc} for the mass of this layer and the corresponding accretion rate $\dot{m}_{acc}$.

- The inner $1.1\,M_\odot$ core of the PNS is cut out and replaced by a contracting inner grid boundary and a corresponding boundary condition in our model. This inner core is considered to be the supranuclear high-density region of the nascent NS, whose detailed physics is still subject to considerable uncertainties. This region is replaced by an analytic description, whose parameters Γ,

$R_c(t)$, and n (see Ugliano et al. 2012) are set to the same values for all stars. This makes sense because the supranuclear phase is highly incompressible, for which reason it can be expected that the volume of the core is not largely different during the explosion phase for different PNS masses. Moreover, the neutrino diffusion time scale out of this core is seconds, which implies that its neutrino emission is of secondary importance during the shorter post-bounce phase when the explosion develops. Despite its simplicity, our core treatment still includes progenitor and accretion dependent variations through the mass m_{acc} of the hot accretion mantle of the PNS and the mass accretion rate $\dot{m}_{acc}$, whose influence on the inner core is accounted for in Eqs. (1)–(4) of Ugliano et al. (2012) for describing the energy evolution of the core model.

- The onset of the explosion is considerably delayed (typically between several $100\,\mathrm{ms}$ and about a second) with a slow (instead of abrupt) rise of the explosion energy during the subsequent shock acceleration phase, when an intense neutrino-driven wind ejects matter and delivers power to the explosion. Neutrino heating cannot deposit the explosion energy impulsively, because the ejected matter needs to absorb enough energy from neutrinos to be accelerated outwards. The rate of energy input to the explosion is therefore limited by the rate at which matter can be channeled trough the heating region. A long-lasting period (hundreds of milliseconds to more than a second) of increasing energy is characteristic of neutrino-driven explosions (Fig. 2) and is observed as gradual growth of the explosion energy also in 2D explosion models, e.g., by Scheck et al. (2006) and Bruenn et al. (2014). To achieve this behavior in our 1D models the core-neutrino source needs to keep up high neutrino luminosities for a more extended period of time than found in fully self-consistent SN simulations, where the rapid decline of the mass-accretion rate at the surface of the iron core and at the interface of silicon and silicon-enriched oxygen layers leads to a strong decrease of the accretion luminosity. The longer period of high neutrino emission is compensated by a somewhat underestimated early post-bounce neutrino luminosity (Fig. 2) in order to satisfy the energy constraints set by the total gravitational binding energy of the forming NS.

- The time scale and duration of the growth of the explosion energy in multi-D models of neutrino-driven SNe are connected to an extended period of continued accretion and simultaneous shock expansion that follows *after* the revival of the stalled shock (see Marek & Janka 2009). Persistent accretion thereby ensures the maintenance of a significant accretion luminosity, while partial re-ejection of accreted and neutrino-heated matter boosts the explosion energy. In our 1D simulations the physics of such a two-component flow cannot be accurately accounted for. In order to approximate the consequences of this truly multi-dimensional phase, our 1D models are constructed with important two properties: On the one hand they refer to a high level of the PNS-core luminosity for about one second. On the other hand they are set up to possess a more extended accretion phase that precedes the onset of the delayed ex-
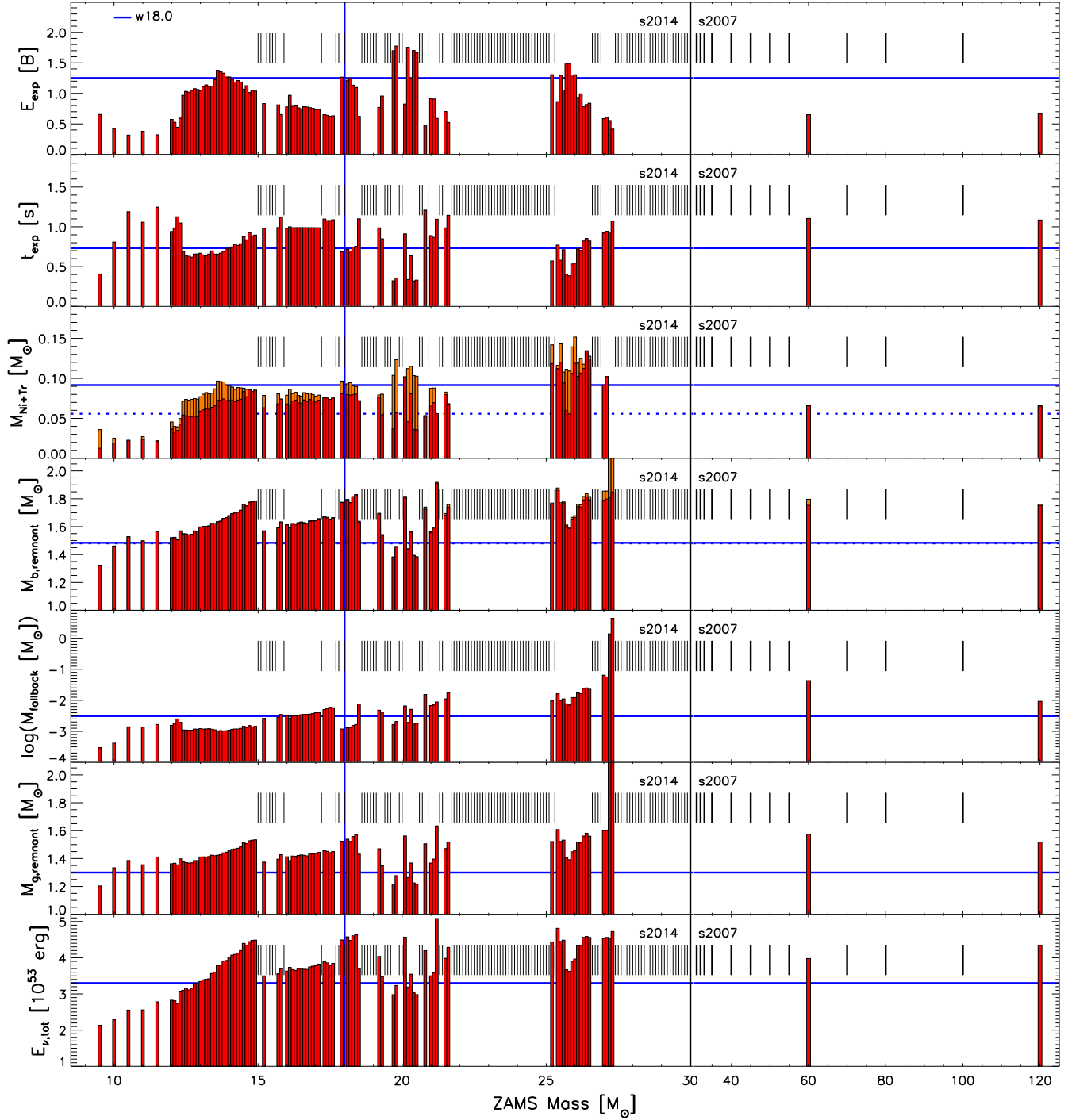
FIG. 3.— Explosion properties for models of the s2014 series, the supplementary low-mass progenitors with $M_{ZAMS} < 15\,M_\odot$, and models with $M_{ZAMS} > 30\,M_\odot$ from the s2007 series, exploded with the w18.0 calibration. A black vertical line marks the boundary between the two progenitor sets. The panels show the final explosion energies, E_{exp} (*top*; 1 B = 1 bethe = 10^{51} erg), times of the onset of the explosion, t_{exp} (defined as the moment when the shock expands beyond 500 km; *second from top*), masses of ejected explosively produced ^{56}Ni (red bars) and tracer element (orange bars; *third from top*), baryonic remnant masses with fallback masses indicated by orange sections of the bars (*fourth from top*), fallback masses (plotted logarithmically; *fifth from top*), gravitational remnant masses (Eq. (10); *sixth from top*), and total energies radiated in neutrinos, $E_{\nu,tot}$ (*bottom*). Mass and parameter values of the calibration models are indicated by vertical and horizontal blue lines, respectively, with the dashed horizontal blue line in the middle panel giving the ^{56}Ni mass and the solid horizontal blue line the sum of ^{56}Ni and tracer. Non-exploding cases are marked by short vertical black bars in the upper half of each panel.

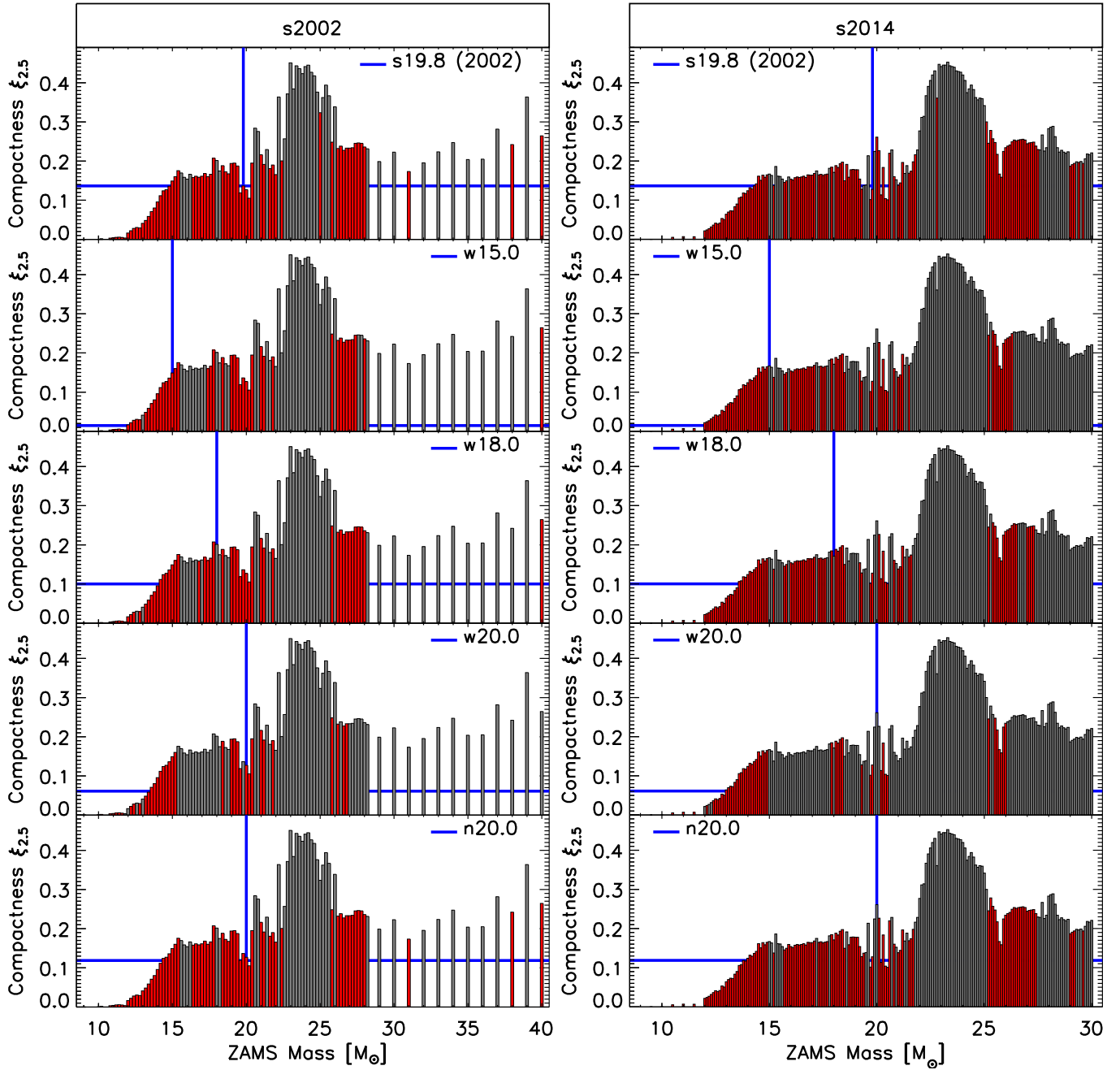FIG. 4.— Compactness $\xi_{2.5}$ versus ZAMS mass for the s2002 (*left*) and s2014 progenitor series (plus $M_{\mathrm{ZAMS}} < 15\,M_\odot$ models) with exploding (red bars) and non-exploding (gray bars) cases for all calibrations. The s2002 results for the s19.8 calibration agree well with Ugliano et al. (2012). Blue vertical and horizontal lines indicate the values of the progenitors used for the calibrations.

plosion before the intense neutrino-driven wind pumps energy into the explosion. The power and mass loss in this wind are overestimated compared to sophisticated neutrino-cooling simulations of PNSs. However, this overestimation of the wind strength has its justification: The early wind is supposed to mimic the mass ejection that is fed in the multi-dimensional case by the inflow and partial re-ejection of matter falling towards the gain radius during the episode of simultaneous accretion and shock expansion. The enhanced wind mass counterbalances the extra mass accretion by the PNS during the long phase before the shock acceleration is launched, and this enhanced wind mass is of crucial importance to carry the energy of the neutrino-powered blast.

Figure 2 shows the post-bounce evolution of the stalled SN shock, the onset of the explosion, energy evolution, and the time evolution of the neutrino emission properties for three representative progenitors, namely s14, s21, and s27 of the s2014 series, which explode successfully with the w18.0 calibration. The shock stagnation at a radius of approximately 200 km lasts between ~700 ms and 900 ms and can exhibit the well-known oscillatory expansion and contraction phases, which signal proximity to the explosion (see e.g., Buras et al. 2006; Murphy & Burrows 2008; Fernández 2012). The explosion sets in shortly after M_4 (Eq. 2) has fallen through the shock and well before the mass shell corresponding to $M_4 + 0.3$ has collapsed. High neutrino luminosities are maintained by high mass accretion rates and, after the onset of the explosion, by a contribution from the core emission (dashed lines in the luminosity panel of Fig. 2) that grows until roughly one second. The current models underestimate the surface luminosity of heavy-lepton neutrinos compared to more sophisticated simulations because of the chosen modest contraction of the inner boundary of the computational grid (which leads to underestimated temperatures in the accretion layer of the PNS) and because neutrino-pair production by nucleon-nucleon bremsstrahlung is not taken into account. We did not upgrade our treatment in this respect because ν_μ and ν_τ are not of immediate relevance for our study since the explosion hinges exclusively on the heating by ν_e and $\bar{\nu}_e$.

Replacing the inner core of the PNS by a contracting inner boundary of the computational mesh introduces a number of free parameters, whose settings allow one to achieve the desired accretion and neutrino-emission behavior as detailed above. On the one hand, our model contains parameters for the prescription of the contraction of the grid boundary, on the other hand there are parameters for the simple high-density core model (cf. Ugliano et al. 2012 and references therein). While the core-model parameters (Γ, ζ, $R_c(t)$, n) regulate the neutrino-emission evolution of the excised, high-density core of the PNS, the prescribed grid-boundary radius, $R_{ib}(t)$, governs the settling of the hot accretion mantle of the PNS. Because of partially compensating influences and dependences, not all of these parameters have a sensitive impact on the outcome of our study. Again, more relevant than a highly accurate description of individual components of the modeling is a reasonable reproduction of the overall properties of the accretion and neutrino emission history of the stalled SN shock and mass accumulating PNS. For example, the moderate increase of the mean neutrino energies with time and their regular hierarchy ($\langle \epsilon_{\nu_e} \rangle < \langle \epsilon_{\bar{\nu}_e} \rangle < \langle \epsilon_{\nu_x} \rangle$; Fig. 2) are not compatible with the most sophisticated current models (Marek & Janka 2009; Müller & Janka 2014, see, e.g.,). They reflect our choice of a

less extreme contraction of the 1.1 $M_\odot$ shell than found in simulations with soft nuclear equations of state for the core matter, where the PNS contracts more strongly and its accretion mantle heats up to higher temperatures at later post-bounce times (compare Scheck et al. 2006 and see the discussion by Pejcha & Thompson 2015). Our choice is motivated solely by numerical reasons (because of less stringent time-step constraints), but it has no immediate drawbacks for our systematic exploration of explosion conditions in large progenitor sets. Since neutrino-energy deposition depends on $L_\nu \langle \epsilon_\nu^2 \rangle$, the underestimated mean neutrino energies at late times can be compensated by higher neutrino luminosities L_ν of the PNS core.

The neutrino emission from the PNS-core region is parametrized in accordance with basic physics constraints. This means that the total loss of electron-lepton number is compatible with the typical neutronization of the inner 1.1 $M_\odot$ core, whose release of gravitational binding energy satisfies energy conservation and virial theorem (see Ugliano et al. 2012). Correspondingly chosen boundary luminosities therefore ensure a basically realistic deleptonization and cooling evolution of the PNS as a whole and of the accretion mantle in particular, where much of the inner-boundary fluxes are absorbed and reprocessed. Again, a proper representation of progenitor-dependent variations requires a reasonable description of the overall system behavior but does not need a very high sophistication of all individual components of the system.

2.3.4. Calibration for low-ZAMS mass range

Agreement with the constraints from SN 1987A employed in our work (i.e., the observed explosion energy, ^{56}Ni mass, total neutrino energy loss, and the duration of the neutrino signal) can be achieved with different sets of values of the PNS core-model parameters. Using only one observed SN case the parameter set is underconstrained and the choice of suitable values is ambiguous. It is therefore not guaranteed that the calibration works equally well in the whole mass range of investigated stellar models.

In particular stars in the low ZAMS-mass regime ($M_{\rm ZAMS} \lesssim$ 12–13 $M_\odot$) possess properties that are distinctly different from those of the adopted SN 1987A progenitors and in the mass neighborhood of these progenitors. Stars with $M_{\rm ZAMS} \lesssim$ 12–13 $M_\odot$ are characterized by very small values of compactness (Eq. 1), binding energy outside of the iron core and outside of M_4 (Eq. 2), and mass derivative μ_4 (Eq. 3). The progenitor of SN 1054 giving birth to the Crab remnant is considered to belong to this mass range, more specifically to have been a star with mass around 10 $M_\odot$ (Nomoto et al. 1982; Smith 2013; Tominaga et al. 2013). Because of their structural similarities and distinctive differences compared to more massive stars, Sukhbold et al. (2015) call progenitors below roughly 12–13 $M_\odot$ "Crab-like" in contrast to stars above this mass limit, which they term "SN 1987-like".

Stars below ~10 $M_\odot$ were found to explode easily in self-consistent, sophisticated 1D, 2D and 3D simulations (Kitaura et al. 2006; Janka et al. 2008; Fischer et al. 2010; Wanajo et al. 2011; Janka et al. 2012; Melson et al. 2015a) with low energies (less than or around 10^{50} erg = 0.1 B) and little nickel production (< 0.01 $M_\odot$), in agreement with observational properties concluded from detailed analyses of the Crab remnant (e.g., Yang & Chevalier 2015). We therefore consider the results of these state-of-the-art SN models together with the empirical constraints for the Crab supernova as important

benchmark that should be reproduced by our approximate 1D modeling of neutrino-powered explosions.

The results of Ugliano et al. (2012) revealed a problem in this respect, because they showed far more energetic explosions of stars in the low-mass domain than expected on grounds of the sophisticated simulations and from observations of Crab. Obviously, the neutrino-source calibration used by Ugliano et al. (2012) is not appropriate to reproduce "realistic" explosion conditions in stars with very dilute shells around the iron core. Instead, it leads to an overestimated power of the neutrino-driven wind and therefore overestimated explosion energies. In particular, the strong and energetic wind is in conflict with the short period of simultaneous postshock accretion and mass ejection after the onset of the explosion in $\lesssim 10\,M_\odot$ stars. Since the mass accretion rate is low and the duration of the accretion phase is limited by the fast shock expansion, the energetic importance of this phase is diminished by the small mass that is channelled through the neutrino-heating layer in convective flows (Kitaura et al. 2006; Janka et al. 2008; Wanajo et al. 2011; Janka et al. 2012; Melson et al. 2015a). In order to account for these features found in the most refined simulations of low-mass stellar explosions, the neutrino-driven wind power of our parametric models has to be reduced.

We realize such a reduction of the wind power by decreasing the parameter ζ, which scales the compression work exerted on the inner (excised) core of the PNS by the overlying accretion mantle (cf. Eqs. 1–4 in Ugliano et al. 2012), in proportionality to the compactness parameter $\xi_{1.75,b}$, which drops strongly for low-mass progenitors (see Eq. 4). This procedure can be justified by the much lighter accretion layers of such stars, which implies less compression of the PNS core by the outer weight. Such a modification reduces the neutrino emission of the high-density core and therefore the mass outflow in the early neutrino-driven wind. As a consequence, the explosion energy falls off towards the low-mass end of the investigated progenitor sets. This can be seen in the upper panel of Fig. 3, which should be compared to the upper left panel of Fig. 5 in Ugliano et al. (2012).

The ζ scaling of Eq. (4) is introduced as a quick fix in the course of this work and is a fairly ad hoc measure to cure the problem of overestimated explosion energies for low-mass SN progenitors. In Sukhbold et al. (2015) a different approach is taken, in which the final value of the core-radius parameter of the one-zone model describing the supernuclear PNS interior as neutrino source (see Ugliano et al. 2012) is modified. This procedure can directly be motivated by the contraction of the PNS found in self-consistent cooling simulations with microphysical high-density equations of state and detailed neutrino transport. Mathematically, the modification of the core radius has a similar effect on the core-neutrino emission as the ζ scaling employed here. While we refer the reader to Sukhbold et al. (2015) for details, we emphasize that the consequences for the overall explosion behavior of the low-mass progenitors is very similar for both the ζ reduction and the core-radius adjustment applied by Sukhbold et al. (2015). They lead to considerably lower explosion energies for $M_{\mathrm{ZAMS}} \lesssim 12\,M_\odot$ stars and a further drop of the explosion energies below ~9.5 $M_\odot$.

As a drawback of this modification, the explosions of some of the low-mass progenitors between ~10.5 $M_\odot$ and ~12.5 $M_\odot$ set in rather late (>1 s p.b., cf. Fig. 3)[5]. This, however, is basically compatible with the tendency of relatively slow shock

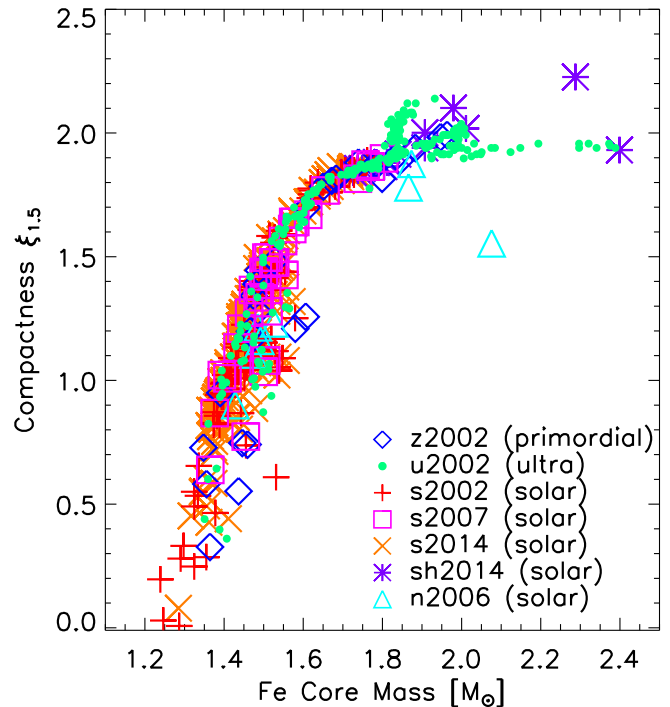[5] In extremely rare cases one may even obtain failed explosions.

FIG. 5.— Correlation of iron-core mass, M_{Fe}, and compactness $\xi_{1.5}$ for the investigated models of all progenitor series. Note that M_{Fe} is taken from the pre-collapse model while $\xi_{1.5}$ is evaluated for a central density of $5 \times 10^{10}\,\mathrm{g\,cm^{-3}}$.

expansion and late explosions that are also found in sophisticated multi-dimensional simulations of such stars, which, in addition, reveal long-lasting phases of simultaneous accretion and mass ejection after the onset of the explosion (Müller et al. 2013; Müller 2015). This extended accretion phase has only moderate consequences for the estimated remnant masses, because the mass accretion rate of these progenitors reaches a low level of $\lesssim 0.05$–$0.1\,M_\odot\,\mathrm{s^{-1}}$ after a few 100 ms post bounce, and some or even most of the accreted mass is re-ejected in the neutrino-driven wind.

Besides providing information on the explosion energies and the onset times of the explosion (defined by the time the outgoing shock reaches 500 km), Fig. 3 also displays for exploding models the ejected masses of ^{56}Ni and iron-group tracer element, the baryonic and gravitational remnant masses, the fallback masses, and the total energies radiated by neutrinos. Overall, these results exhibit features very similar to those discussed in detail by Ugliano et al. (2012) for a different progenitor series and a different calibration model. We point out that the fallback masses in the low-mass range of progenitors were overestimated by Ugliano et al. (2012) due to an error in the analysis (more discussion will follow in Sect. 3.5; an erratum on this aspect is in preparation.)

3. RESULTS

3.1. *One and two-parameter classifications*

Figure 4 shows $\xi_{2.5}$ versus ZAMS mass with BH formation cases indicated by gray and explosions by red bars for the s2002 and s2014 series and all calibrations. The irregular pattern found by Ugliano et al. (2012) for the s2002 progenitors is reproduced and appears similarly in the s2014 set. High compactness $\xi_{2.5}$ exhibits a tendency to correlate with BHs. But also other parameters reflect this trend, for exam-
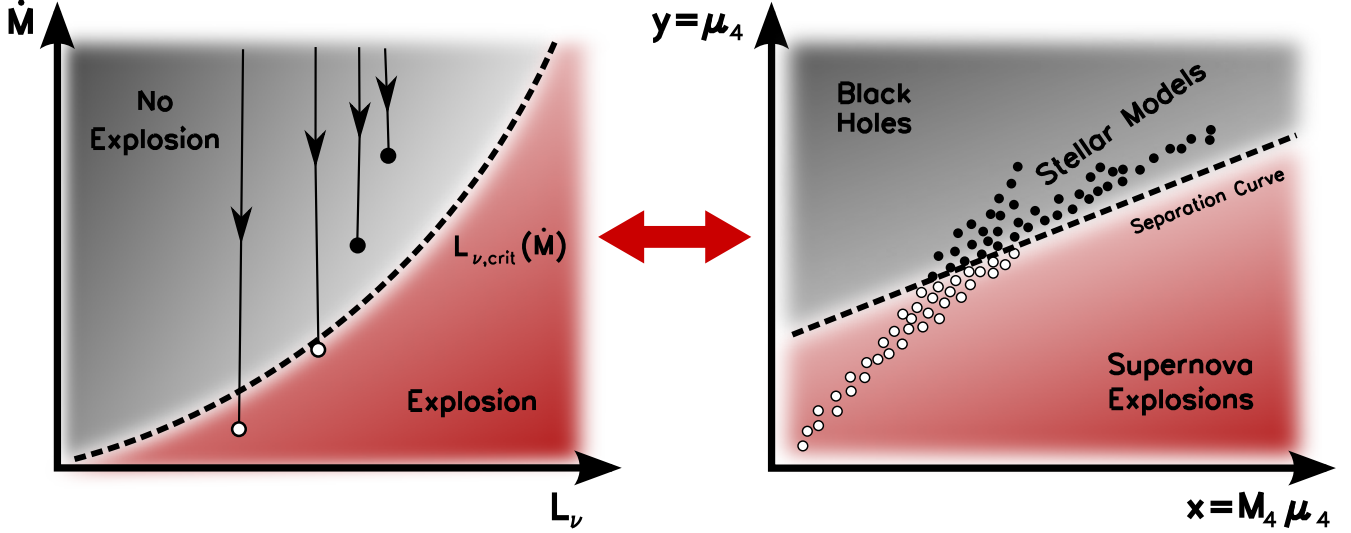
FIG. 6.— Correspondence of L_ν-$\dot{M}$ plane with critical neutrino luminosity $L_{\nu,\text{crit}}(\dot{M})$ (*left*) and x-y plane with separation curve $y_{\text{sep}}(x)$ (*right*). In the left plot post-bounce evolution paths of successfully exploding models (white circles) and non-exploding models (black circles) are schematically indicated, corresponding to white and black circles for pre-collapse models in the right plot. Evolution paths of successful models cross the critical line at some point and the accretion ends after the explosion has taken off. In contrast, the tracks of failing cases never reach the critical conditions for launching the runaway expansion of the shock. The symbols in the left plot mark the "optimal point" relative to the critical curve that can be reached, corresponding to the stellar conditions described by the parameters $(M_4\mu_4, \mu_4)$ at the $s = 4$ location, which seems decisive for the success or failure of the explosion of a progenitor, because the accretion rate drops strongly outside.

ple $\xi_{1.5}$, the iron-core mass M_{Fe} (defined as the core where $\sum_{\{i|A_i>46\}} X_i > 0.5$ for nuclei with mass numbers A_i and mass fractions X_i), and the enclosed mass at the bottom of the O-burning shell. All three of them are tightly correlated, see Fig. 5 as well as Fig. 4 of Ugliano et al. (2012). Also high values of the binding energy $E_b(m > M_{\text{Fe}})$ outside of M_{Fe} signals a tendency for BH formation, because this energy correlates with $\xi_{2.5}$ (cf. Fig. 4 in Ugliano et al. 2012). However, for none of these single parameters a sharp boundary value exists that discriminates between explosions and non-explosions. For all such choices of a parameter, the BH formation limit tends to vary (non-monotonically) with M_{ZAMS} and in a broad interval of values either explosion or BH formation can happen. Pejcha & Thompson (2015) tried to optimize the choice of M for ξ_M, but even their best case achieved only 88% of correct predictions. Since in the cases of $\xi_{2.5}$ and $E_b(m > M_{\text{Fe}})$, for example, the threshold value for BH formation tends to grow with higher ZAMS mass, one may hypothesize that a second parameter could improve the predictions.

Placing the progenitors in a two-parameter space spanned by $\xi_{1.5}$ and $\xi_{2.5}$ or, equally good, M_{Fe} and $\xi_{2.5}$, begins to show a cleaner separation of successful and failed explosions: SNe are obtained for small values of $\xi_{2.5}$, whereas BHs are formed for high values of $\xi_{2.5}$, but the value of this threshold increases with $\xi_{1.5}$ and M_{Fe}. For given $\xi_{1.5}$ (or M_{Fe}) there is a value of $\xi_{2.5}$ above which only BHs are formed. However, there is still a broad overlap region of mixed cases.

This beginning separation can be understood in view of the theoretical background of the neutrino-driven mechanism, where the expansion of the SN shock is obstructed by the ram pressure of infalling stellar-core matter and shock expansion is pushed by neutrino-energy deposition behind the shock. For neutrino luminosities above a critical threshold $L_{\nu,\text{crit}}(\dot{M})$, which depends on the mass-accretion rate $\dot{M}$ of the shock, shock runaway and explosion are triggered by neutrino heating (see Fig. 6, left panel, and, e.g., Burrows & Goshy 1993; Janka 2001; Murphy & Burrows 2008; Nord-

haus et al. 2010; Hanke et al. 2012; Fernández 2012; Pejcha & Thompson 2012; Janka 2012; Müller & Janka 2015). M_{Fe} (or $\xi_{1.5}$) can be considered as a measure of the mass M_{ns} of the PNS as accretor, which determines the strength of the gravitational potential and the size of the neutrino luminosities. Such a dependence can be concluded from the proportionality $L_\nu \propto R_\nu^2 T_\nu^4$, where R_ν is the largely progenitor-independent neutrinosphere radius and the neutrinospheric temperature T_ν increases roughly linearly with M_{ns} (see Müller & Janka 2014). On the other hand, the long-time mass-accretion rate of the PNS grows with $\xi_{2.5}$, which is higher for denser stellar cores. For each PNS mass explosions become impossible above a certain value of $\dot{M}$ or $\xi_{2.5}$.

3.2. Two-parameter classification based on the theoretical concept of the neutrino-driven mechanism

If the initial mass cut at the onset of the explosion develops at an enclosed mass $M = m(r)$ of the progenitor, we can choose $M = m(r)$ as a suitable proxy of the initial PNS mass, M_{ns}. A rough measure of the mass-accretion rate $\dot{M}$ by the stalled shock around the onset of the explosion is then given by the mass-gradient $m'(r) \equiv \mathrm{d}m(r)/\mathrm{d}r = 4\pi r^2 \rho(r)$ at the corresponding radius r. This is the case because $m'(r)$ can be directly linked to the free-fall accretion rate of matter collapsing into the shock from initial radius r according to

$$\dot{M} = \frac{\mathrm{d}m}{\mathrm{d}t_{\text{ff}}} = \frac{\mathrm{d}m(r)}{\mathrm{d}r}\left(\frac{\mathrm{d}t_{\text{ff}}(r)}{\mathrm{d}r}\right)^{-1}$$
$$= \frac{2m'(r)}{t_{\text{ff}}[(3/r) - m'(r)/m(r)]} \approx \frac{2}{3}\frac{r}{t_{\text{ff}}}m'(r), \quad (5)$$

where $t_{\text{ff}} = \sqrt{r^3/[Gm(r)]}$ is the free-fall timescale (Suwa et al. 2014) and the last, approximate equality is justified by the fact that $(m'/m)^{-1} = \mathrm{d}r/\mathrm{d}\ln(m) \gg r$ outside of the dense stellar core.

Following the critical-luminosity concept now points the way to further improvements towards a classification scheme

of explosion conditions: The L_ν-$\dot{M}$ dependence of the neutrino-driven mechanism suggests that the explodability of the progenitors may be classified by the parameters $M = m(r)$ and $\dot{M} \propto m'(r)$, because the accretion luminosity $L_\nu^{\mathrm{acc}} \propto GM_{\mathrm{ns}}\dot{M}/R_{\mathrm{ns}} \propto Mm'(r)$ accounts for a major fraction of the neutrino luminosity of the PNS at the time of shock revival (Müller & Janka 2014; Müller & Janka 2015), and, in particular, it is the part of the neutrino emission that reflects the main progenitor dependence. It is important to note that the time-evolving NS and neutrinospheric radii, $R_{\mathrm{ns}} \sim R_\nu$, are nearly the same for different progenitors and only weakly time dependent when the explosions take place rather late after bounce. This is true for our simulations (where $t_{\mathrm{exp}} \gtrsim 0.5\,\mathrm{s}$ with few exceptions; Fig. 3) as well as for self-consistent, sophisticated models (see, e.g., Fig. 3 in Müller & Janka 2014). In both cases the spread of the NS radii and their evolution between ~0.4 s and 1 s after bounce accounts for less than 25% variation around an average value of all investigated models. In Sect. 3.6 we will come back to this argument and give reasons why the NS radius has little influence on the results discussed in this work. Moreover, the neutrino loss from the low-entropy, degenerate PNS core, whose properties are determined by the incompressibility of supranuclear matter, should exhibit a progenitor dependence mostly through the different weight of the surrounding accretion mantle, whose growth depends on $\dot{M}$. Such a connection is expressed by the terms depending on m_{acc} and $\dot{m}_{\mathrm{acc}}$ in the neutrino luminosity of the high-density PNS core in Eq. (4) of Ugliano et al. (2012). We therefore hypothesize, and demonstrate below, a correspondence of the L_ν-$\dot{M}$ space and the Mm'-m' parameter plane and expect that the critical luminosity curve $L_{\nu,\mathrm{crit}}(\dot{M})$ maps to a curve separating BH formation and successful explosions in the Mm'-m' plane[6].

In our simulations neutrino-driven explosions set in around the time or shortly after the moment when infalling matter arriving at the shock possesses an entropy $s \sim 4$. We therefore choose M_4 (Eq. 2) as our proxy of the PNS mass, $M_4 \propto M_{\mathrm{ns}}$, and $\mu_4 \equiv m'(r)[M_\odot/(1000\,\mathrm{km})]^{-1}|_{s=4}$ (Eq. 3) as corresponding measure of the mass-accretion rate at this time, $\mu_4 \propto \dot{M}$. The product Mm' is therefore repesented by $M_4\mu_4$. Tests showed that replacing M_4 by the iron-core mass, M_{Fe}, is similarly good and yields results of nearly the same quality in the analysis following below (which points to an underlying correlation between M_4 and M_{Fe}). In practice, we evaluate Eq. (3) for μ_4 by the average mass-gradient of the progenitor just outside of $s = 4$ according to

$$\mu_4 \equiv \left.\frac{\Delta m/M_\odot}{\Delta r/1000\,\mathrm{km}}\right|_{s=4}$$
$$= \frac{(M_4 + \Delta m/M_\odot) - M_4}{[r(M_4 + \Delta m/M_\odot) - r(s = 4)]/1000\,\mathrm{km}}, \quad (6)$$

with $\Delta m = 0.3\,M_\odot$ yielding optimal results according to tests with varied mass intervals Δm. With the parameters M_4 and μ_4 picked, our imagined mapping between critical conditions in the L_ν-$\dot{M}$ and Mm'-m' spaces transforms into such a mapping

---

[6] Since the shock revival is determined by neutrino heating, which depends on $L_\nu\langle\epsilon_\nu^2\rangle$, and since the average squared neutrino energy $\langle\epsilon_\nu^2\rangle \propto T_\nu^2 \propto M_{\mathrm{ns}}^2$ increases with time and PNS mass (Müller & Janka 2014), Müller & Janka (2015) discuss the critical condition for shock revival in terms of $L_\nu\langle\epsilon_\nu^2\rangle$ as a function of $M_{\mathrm{ns}}\dot{M}$. This suggests that an alternative choice of parameters could be M^3m' and Mm' instead of Mm' and m', respectively. Our results demonstrate that the basic physics is already captured by the Mm'-m' dependence.

---

relation between the L_ν-$\dot{M}$ and $M_4\mu_4$-μ_4 planes as illustrated by Fig. 6.

Figure 7 demonstrates the strong correlation of the mass accretion rate $\dot{M} = \mathrm{d}m/\mathrm{d}t$ with the parameter μ_4 as given by Eq. (6) (panel c) as well as the tight correlations between $M_4\mu_4$ and the sum of ν_e and $\bar{\nu}_e$ luminosities (panel a) and the summed product of the luminosities and mean squared energies of ν_e and $\bar{\nu}_e$ (panel b). It is important to note that the non-stationarity of the conditions requires us to average the quantities plotted on the abscissas over time from the moment when the $s = 4$ interface passes through the shock until the models either explode (i.e., the shock radius expands beyond 500 km; open circles) or until the mass shell $(M_4 + 0.3)\,M_\odot$ has fallen through the shock, which sets an endpoint to the time interval within which explosions are obtained (non-exploding cases marked by filled circles). The time averaging is needed not only because of evolutionary changes of the preshock mass-accretion rate (as determined by the progenitor structure) and corresponding evolutionary trends of the emitted neutrino luminosities and mean energies. The averaging is necessary, in particular, because the majority of our models develops large-amplitude shock oscillations after the accretion of the $s = 4$ interface, which leads to quasi-periodic variations of the neutrino emission properties with more or less pronounced, growing amplitudes (see the examples in Fig. 2). Panel d demonstrates that exploding models (open circles) exceed a value of unity for the ratio of advection time scale, t_{adv}, to heating time scale, t_{heat}, in the gain layer, which was considered as a useful critical threshold for diagnosing explosions in many previous works (e.g., Janka & Keil 1998; Thompson 2000; Janka et al. 2001; Thompson et al. 2005; Buras et al. 2006; Marek & Janka 2009; Müller et al. 2012b; Müller & Janka 2015; Fernández 2012). The exploding models also populate the region towards low mass-accretion rates (as visible in panels a–c, too), which confirms our observation reported in Sect. 3.1. In contrast, non-exploding models cluster, clearly separated, in the left, upper area of panel d, where $t_{\mathrm{adv}}/t_{\mathrm{heat}} \lesssim 1$ and the mass-accretion rate tends to be higher. For the calculation of the time scales we follow the definitions previously used by, e.g., Buras et al. (2006), Marek & Janka (2009), Müller et al. (2012b), Müller & Janka (2015):

$$t_{\mathrm{heat}} = \left(\int_{R_{\mathrm{g}}}^{R_{\mathrm{s}}} (e + \Phi)\rho\,\mathrm{d}V\right)\left(\int_{R_{\mathrm{g}}}^{R_{\mathrm{s}}} \dot{q}_\nu\rho\,\mathrm{d}V\right)^{-1}, \quad (7)$$

$$t_{\mathrm{adv}} = \int_{R_{\mathrm{g}}}^{R_{\mathrm{s}}} \frac{1}{|v_r|}\,\mathrm{d}r. \quad (8)$$

Here, the volume and radius integrals are performed over the gain layer between gain radius R_{g} and shock radius R_{s}. e is the sum of the specific kinetic and internal energies, Φ the (Newtonian) gravitational potential, ρ the density, $\dot{q}_\nu$ the net heating rate per unit of mass, and v_r the velocity of the flow. Again, because of the variations of the diagnostic quantities associated with the time evolution of the collapsing star and the oscillations of the gain layer, the mass-accretion rate and time-scale ratio are time-averaged between the moment when the $s = 4$ interface passes the shock until either 300 ms later or until the model explodes (shock radius exceeding 500 km)[7]. Panels e (and f) lend support to the concept of a critical threshold luminosity in the L_ν-$\dot{M}$ (and $L_\nu\langle\epsilon_\nu^2\rangle$-$\dot{M}$) space mentioned

---

[7] We tested intervals ranging from 100 ms to 600 ms and observed the same trends for all choices.
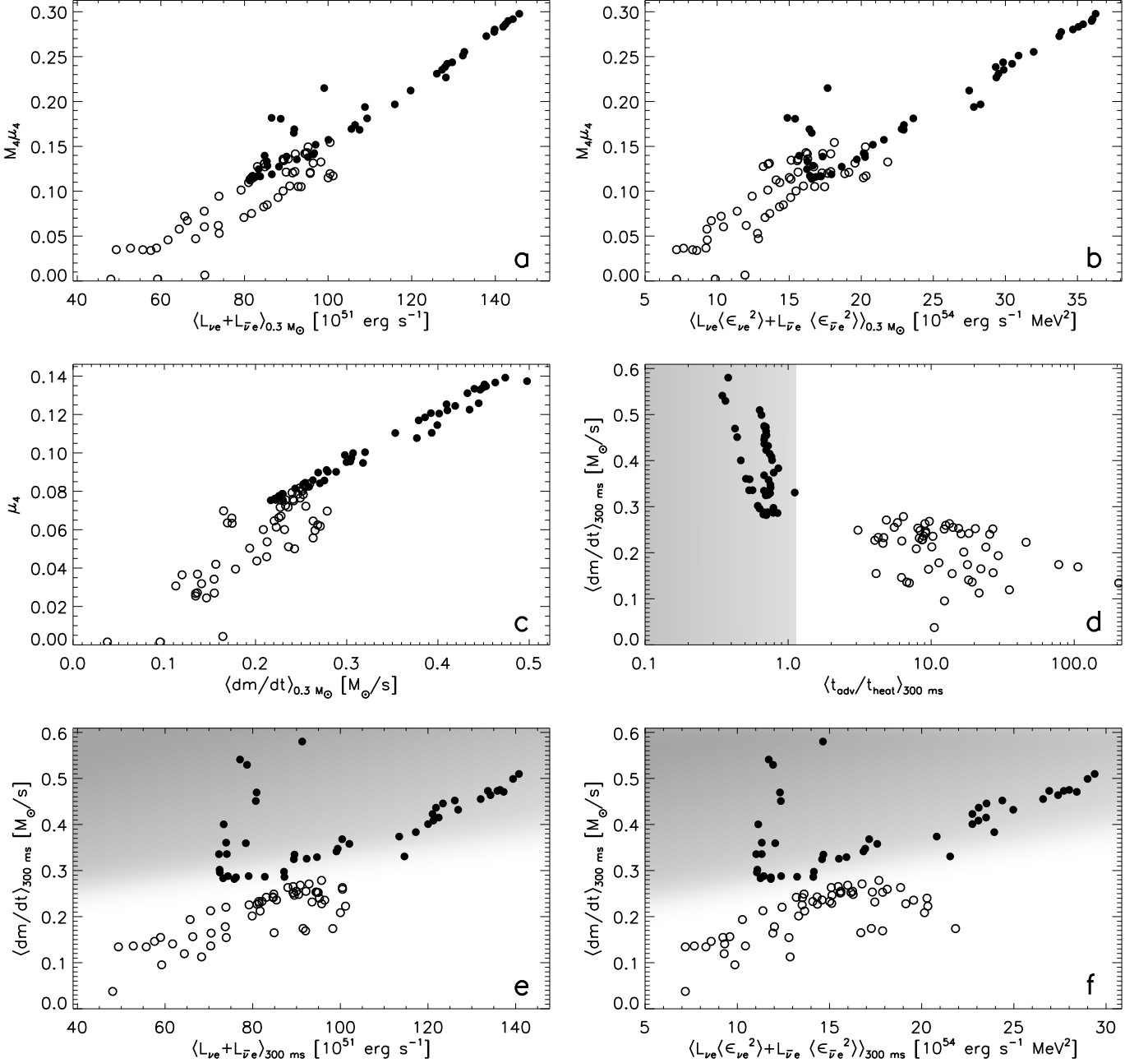
FIG. 7.— End points of the postbounce evolution of exploding (open circles) and non-exploding models (filled circles) in planes spanned by various pairs of parameters. The data correspond to results of the s2002 model series with w18.0 calibration. All symbols represent time-averaged locations because of strong temporal variations of the postshock accretion layer. *Panels a–c* display correlations of our dimensionless progenitor parameters μ_4 and $M_4\mu_4$ with time-averaged values of the preshock mass accretion rate, $\dot{M} = dm/dt$, and the characteristic neutrino-emission properties, respectively, as obtained in our simulations and measured at 500 km. The abscissas of *panels a and b* show the summed luminosities of ν_e and $\bar{\nu}_e$, $L_{\nu_e} + L_{\bar{\nu}_e}$, and the summed products of luminosities and mean squared energies, $L_{\nu_e}\langle\epsilon_{\nu_e}^2\rangle + L_{\bar{\nu}_e}\langle\epsilon_{\bar{\nu}_e}^2\rangle$, of both neutrino species, respectively. For the exploding models the time averaging is performed from the arrival of the $s = 4$ interface at the shock until the explosion sets in (defined by the shock radius reaching 500 km), whereas the averages for non-exploding models cover the time from the $s = 4$ interface passing the shock until 0.3 $M_\odot$ of overlying material have been accreted by the shock. *Panel d* displays the separation of exploding and non-exploding models in the plane spanned by the mass-accretion rate and the ratio of advection to heating time scale. *Panels e and f* demonstrate this separation in the planes spanned by $\dot{M}$ and $L_{\nu_e} + L_{\bar{\nu}_e}$ or $L_{\nu_e}\langle\epsilon_{\nu_e}^2\rangle + L_{\bar{\nu}_e}\langle\epsilon_{\bar{\nu}_e}^2\rangle$, respectively. The time averages of the quantities in *panels d–f* are computed from the passage of the $s = 4$ interface through the shock until 300 ms later for non-exploding models or until the onset of the explosion otherwise. Gray shading in *panels d–f* indicates the regions where explosions fail. (No exact boundary curves are determined for the cases of *panels e and f*.)

above. The two plots show a separation of exploding (open circles) and non-exploding (filled circles) models in a plane spanned by the time-averaged values of the preshock mass accretion rate on the one hand and the sum of ν_e and $\bar{\nu}_e$ luminosities (panel e) or the summed product of ν_e and $\bar{\nu}_e$ luminosities times their mean squared energies on the other hand (panel f). Again the same time-averaging procedure as for panel d is applied. After the $s = 4$ progenitor shell passes the shock, the time-averaged conditions of the exploding models reach the lower halfs of these panels, whereas the time-averaged properties of the non-exploding models define the positions of these unsuccessful explosions in the upper halfs. A separation appears that can be imagined to resemble the critical luminosity curve $L_{\nu,\text{crit}}(\dot{M})$ sketched in the left panel of Fig. 6.

Because of the strong time dependence of the postshock conditions and of the neutrino emission during the phase of dynamical shock expansion and contraction after the accretion of the $s = 4$ interface, it is very difficult to exactly determine the critical luminosity curve that captures the physics of our exploding 1D simulations. Although we do not consider such an effort as hopeless if the governing parameters are carefully taken into account (cf., e.g., the discussions in Pejcha & Thompson 2015; Müller & Janka 2015) and their time variations are suitably averaged, we think that the clear separation of successful and failed explosions visible in panels e and f of Fig. 7 provides proper and sufficient support for the notion of such a critical curve (or, more general: condition) in the $L_{\nu,\text{crit}}$-$\dot{M}$ space. Figure 6 illustrates our imagined relation between the evolution tracks of collapsing stellar cores that explode or fail to explode in this L_{ν}-$\dot{M}$ space on the left side and the locations of SN-producing and BH-forming progenitors in the $M_4\mu_4$-μ_4 plane on the right side. The sketched evolution paths are guided by our results in panels e and f of Fig. 7. In the following section we will demonstrate that exploding and non-exploding simulations indeed separate in the $M_4\mu_4$-μ_4 parameter space.

3.3. *Separation line of exploding and non-exploding progenitors*

The existence of a separation line between BH forming and SN producing progenitors in the $M_4\mu_4$-μ_4 plane is demonstrated by Fig. 8, which shows the positions of the progenitors for all investigated model series in this two-dimensional parameter space. For all five calibrations successful explosions are marked by colored symbols, whereas BH formation is indicated by black symbols. The regions of failed explosions are underlaid by gray. They are bounded by straight lines with fit functions as indicated in the panels of Fig. 8,

$$y_{\text{sep}}(x) = k_1 \cdot x + k_2 , \qquad (9)$$

where $x \equiv M_4\mu_4$ and $y \equiv \mu_4$ are dimensionless variables with M_4 in solar masses and μ_4 computed by Eq. (6). The values of the dimensionless coefficients k_1 and k_2 as listed in Table 2 are determined by minimizing the numbers of outliers.

The stellar models of all progenitor sets populate a narrow strip in the x-y plane of Fig. 8, left panels. BH formation cases are located in the upper left part of the x-y plane. The inclination of the separation line implies that the explosion limit in terms of μ_4 depends on the value of the $M_4\mu_4$ and therefore a single parameter would fail to predict the right behavior in a large number of cases. Denser cores outside of M_4 with high mass-accretion rates (larger μ_4) prevent explosions above some limiting value. This limit grows for more massive

TABLE 2
BH-SN SEPARATION CURVES FOR ALL CALIBRATION MODELS

Calibration Model	k_1 [a]	k_2 [a]	M_4 [b]	μ_4 [b]	$M_4\mu_4$ [b]
s19.8 (2002)	0.274	0.0470	1.529	0.0662	0.101
w15.0 [c]	0.225	0.0495	1.318	0.0176	0.023
w18.0	0.283	0.0430	1.472	0.0530	0.078
w20.0	0.284	0.0393	1.616	0.0469	0.076
n20.0	0.194	0.0580	1.679	0.0441	0.074

[a] Fit parameters of separation curve (Eq. 9) when x and y are measured for a central stellar density of 5×10^{10} g cm^{-3}.

[b] Measured for a central stellar density of 5×10^{10} g cm^{-3}.

[c] M_4 and μ_4 measured roughly at core bounce, because pre-collapse data are not available.

cores and thus higher M_4 because larger mass-accretion rates do not only hamper shock expansion by higher ram pressure but larger core masses and bigger accretion rates also correlate with an increase of the neutrino luminosity of the PNS as expressed by our parameter $M_4\mu_4$. The evolution tracks of successful explosion cases in the left panel of Fig. 6 indicate that for higher $L_\nu \propto M_{\text{ns}}\dot{M}$ the explosion threshold, $L_{\nu,\text{crit}}(\dot{M})$, can be reached for larger values of $\dot{M}$.

Explosions are supported by the combination of a massive PNS, which is associated with a high neutrino luminosity from the cooling of the accretion mantle, on the one hand, and a rapid decline of the accretion rate, which leads to decreasing ram pressure, on the other hand. A high value of M_4 combined with a low value of μ_4 is therefore favorable for an explosion because a high accretion luminosity (due to a high accretor mass $M_{\text{ns}} \approx M_4$) comes together with a low mass accretion rate (and thus low ram pressure and low binding energy) exterior to the $s = 4$ interface (cf. Fig 9). Such conditions are met, and explosions occur readily, when the entropy step at the $s = 4$ location is big, because a high entropy value outside of M_4 correlates with low densities and a low accretion rate. M_4 is usually the base of the oxygen shell and a place where the entropy changes discontinuously causing (or resulting from) a sudden decrease in density due to burning there. This translates into an abrupt decrease in $\dot{M}$ when the mass M_4 accretes. Figure 14 of Sukhbold & Woosley (2014) shows a strong correlation between compactness $\xi_{2.5}$ and location of the oxygen shell. The decrease of the mass accretion rate is abrupt only if the entropy change is steep with mass, for which μ_4 at M_4 is a relevant measure.

Progenitors with $M_{\text{ZAMS}} \lesssim 22\,M_\odot$ that are harder to explode often have relatively small values of M_4 and an entropy ledge above $s = 4$ on a lower level than the entropy reached in more easily exploding stars. The lower neutrino luminosity associated with the smaller accretor mass in combination with the higher ram pressure can prohibit shock expansion in many of these cases. Corresponding to the relatively small values of M_4 and relatively higher densities outside of this mass, these cases stick out from their neighboring stars with respect to the binding energy of overlying material, namely, non-exploding models in almost all cases are characterized by *local* maxima of $E_{\text{b},4} = E_{\text{b}}(m/M_\odot > M_4)$ (see Fig. 9).

In view of this insight it is not astonishing that exploding and non-exploding progenitors can be seen to start separating from each other in the two-parameter space spanned by M_4 and the average entropy value $\langle s \rangle_4$ just outside of M_4 (Fig. 10). Averaging s over the mass interval $[M_4, M_4 + 0.5]$ turns out to yield the best results. Exploding models cluster towards the side of high $\langle s \rangle_4$ and low M_4, while failures are found preferentially for low values of $\langle s \rangle_4$. The threshold
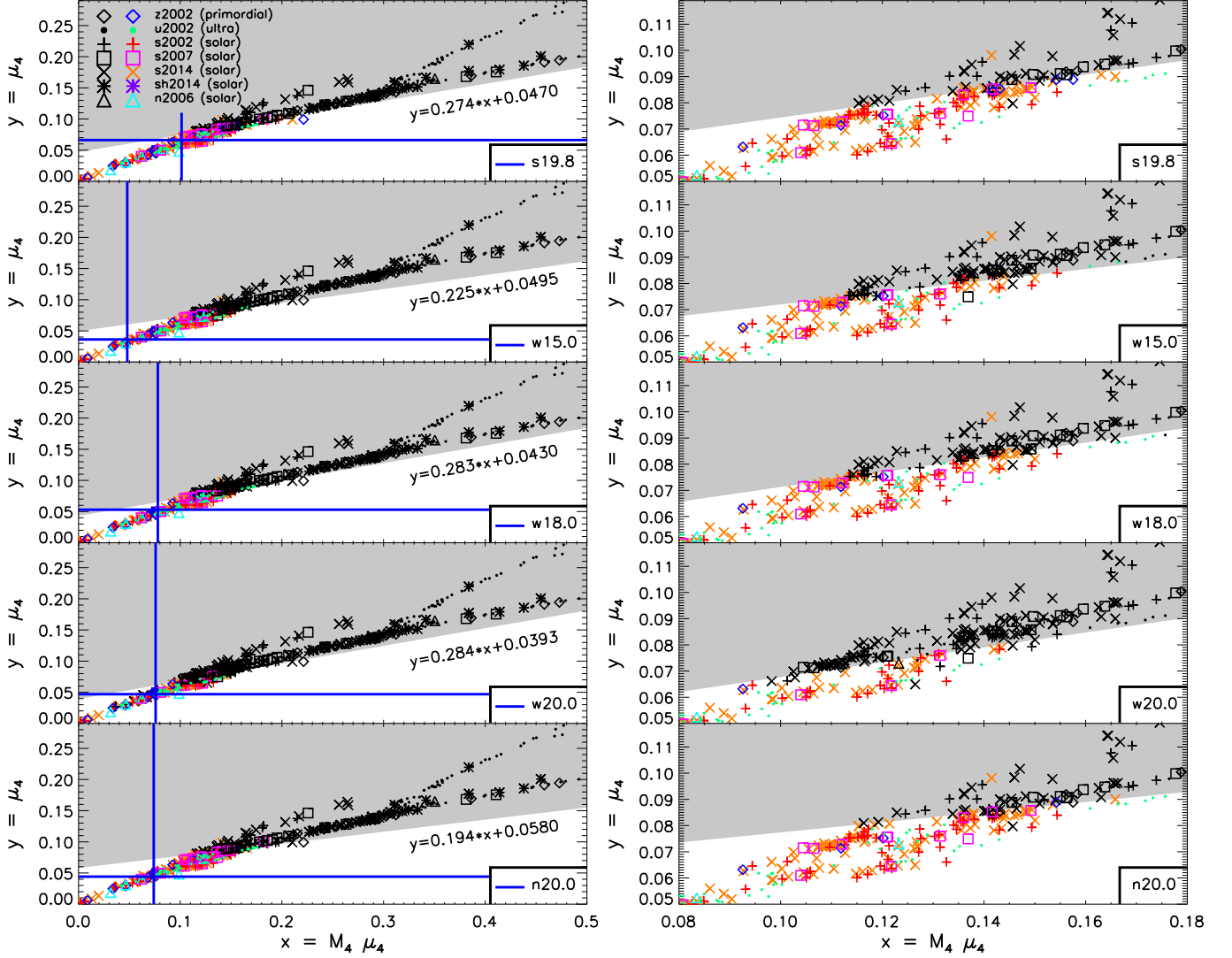
Fig. 8.— Separation curves between BH formation (gray region, black symbols) and SN explosions (white region, colored symbols) for all calibrations in the plane of parameters $x = M_4\mu_4$ and $y = \mu_4$ (zooms in *right* panels). Note that the left panels do not show roughly two dozen BH-forming models of the u2002 series, which populate the x-range between 0.5 and 0.62 and are off the displayed scale. Different symbols and colors correspond to the different progenitor sets. The locations of the calibration models are also indicated in the left panels by crossing blue lines.

for success tends to grow with M_4. However, there is still a broad band where both types of outcomes overlap. The disentanglement of SNe and BH-formation events is clearly better achieved by the parameter set of $M_4\mu_4$ and μ_4, which, in addition, applies correctly not only for stars with $M_{\mathrm{ZAMS}} \geq 15\,M_\odot$ but also for progenitors with lower masses.

3.4. *Stellar outliers*

Out of 621 simulated stellar models for the s19.8, w15.0, w18.0, w20.0, and n20.0 calibrations only 9, 14, 16, 11, and 9 models, respectively, do not follow the behavior predicted by their locations on the one or the other side of the separation line in the $M_4\mu_4$-μ_4 plane (see the zooms in the right column of Fig. 8). But most of these cases lie very close to the boundary curve and their explosion or non-explosion can be affected by fine details and will certainly depend on multi-dimensional effects. A small sample of outliers is farther away from the boundary line. The w20.0 calibration is the weakest driver of neutrino-powered explosions in our set and tends to yield the largest number of such more extreme outliers.

These cases possess unusual structural features that influence their readiness to explode. On the non-exploding side of the separation line, model s20.8 of the s2014 series with $(M_4\mu_4, \mu_4) \approx (0.142, 0.0981)$ is one example of a progenitor that blows up with all calibrations except w20.0, although it is predicted to fail (see Fig. 8). In contrast, its mass-neighbor s20.9 with $(M_4\mu_4, \mu_4) \approx (0.123, 0.085)$ as well as its close neighbor in the $M_4\mu_4$-μ_4 space, s15.8 of the s2002 series with $(M_4\mu_4, \mu_4) \approx (0.140, 0.096)$, both form BHs as expected. The structure of these pre-supernova models in the $s = 4$ region is very similar with $M_4 = 1.45, 1.45, 1.46$ for s20.8, s20.9, s15.8, respectively. Although s20.8 reaches a lower entropy level outside of $s = 4$ than the other two cases and therefore is also predicted to fail, its explosion becomes possible when the next entropy step at an enclosed mass of $1.77\,M_\odot$ reaches the shock. This step is slightly farther out (at $1.78\,M_\odot$) in the s20.9 case and comes much later (at $\sim 1.9\,M_\odot$) in the s15.8 model. Both the earlier entropy jump and the lower preceding entropy level enable the explosion of s20.8, because the associated higher density maintains a higher mass-accretion
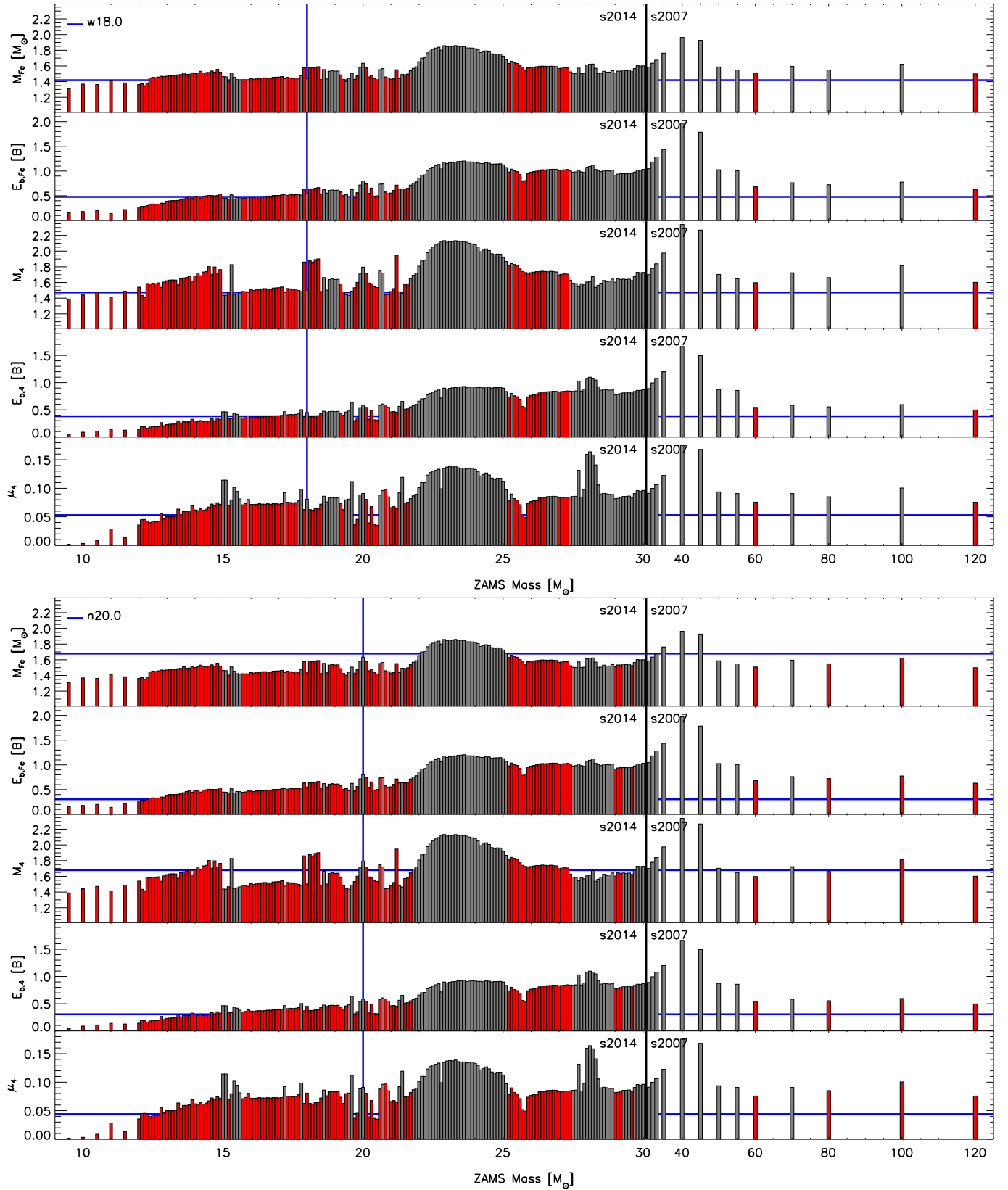
FIG. 9.— Iron-core masses M_{Fe} (*top panel*), exterior binding energies ($E_{b,Fe} = E_b(m > M_{Fe})$; *second panel*), normalized masses M_4 (*third panel*), exterior binding energies ($E_{b,4} = E_b(m/M_\odot > M_4)$; *fourth panel*), and μ_4 (*fifth panel*), for models of the s2014 series, the supplementary low-mass progenitors with $M_{ZAMS} < 15\,M_\odot$, and models with $M_{ZAMS} > 30\,M_\odot$ from the s2007 series. A black vertical line marks the boundary between the two progenitor sets. Red bars indicate exploding cases and gray bars non-exploding ones. All quantities are measured when the central density of the collapsing stellar iron core is $5 \times 10^{10}\,\mathrm{g\,cm^{-3}}$. The *upper five panels* correspond to the w18.0 calibration, the *lower five panels* to the n20.0 calibration. Mass and parameter values of the calibration models are indicated by vertical and horizontal blue lines, respectively. In the region of $M_{ZAMS} \lesssim 22\,M_\odot$ non-exploding cases, with very few exceptions, correlate with local minima of M_4 and pronounced local maxima of μ_4 and $E_{b,4}$. A high value of M_4 combined with a low value of μ_4 is typically supportive for an explosion because a high accretion luminosity (due to a high accretor mass $M_{ns} \approx M_4$) comes together with a low mass accretion rate (and thus low ram pressure and low binding energy) exterior to the $s = 4$ interface. The iron-core masses and their exterior binding energies show a similar tendency, but significantly less pronounced.
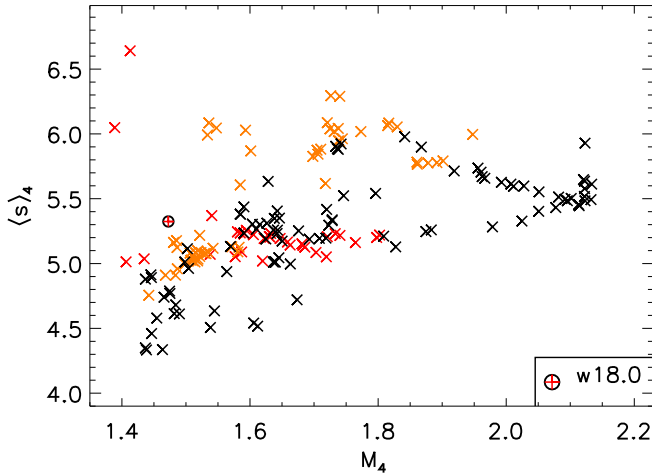
FIG. 10.— Two-parameter plane spanned by $M_4 = M(s = 4)$ and mean entropy of overlying matter, $\langle s \rangle_4$, averaged over a mass intervall of $0.5\,M_\odot$. The locations of progenitors from the s2014 series and the supplementary low-mass set with $M_{ZAMS} < 15\,M_\odot$ are marked by crosses. Black crosses indicate BH formation cases and tend to concentrate towards the lower and right half of the panel, i.e., towards low values of $\langle s \rangle_4$ for given M_4. Orange crosses mean successful SN explosions of the s2014 models with the w18.0 calibration, and red crosses are explosions for the $M_{ZAMS} < 15\,M_\odot$ progenitors. While high entropies outside of the $s = 4$ location signal a tendency of success for the stars of the s2014 set (although the separation from BH-formation cases is not sharp), the successfully exploding $M_{ZAMS} < 15\,M_\odot$ models mix completely with BH forming events.

FIG. 11.— ZAMS masses, iron-core masses, M_{Fe}, and binding energies outside of the iron core, $E_b(m > M_{Fe})$, (from top to bottom) of the s2014 series and the supplementary low-mass progenitors with $M_{ZAMS} < 15\,M_\odot$ in the x-y parameter plane. The solid and dashed lines mark the separation curves $y_{sep}(x)$ for the w18.0 and n20.0 calibration models (different symbols as given in the legend), respectively.

rate and therefore higher neutrino luminosity until the entropy jump at $1.77\,M_\odot$ falls into the shock. The abnormal structure of the progenitor therefore prevents that the explosion behavior is correctly captured by our two-parameter criterion for the explodability.

On the exploding side, model s15.3 of the s2014 series with $(M_4\mu_4, \mu_4) \approx (0.146, 0.0797)$ is expected to blow up according to the two-parameter criterion, but does not do so for all calibrations (Fig. 8). Similarly, s15.0 of the s2007 series with $(M_4\mu_4, \mu_4) \approx (0.137, 0.0749)$ fails with the w15.0 and w20.0 calibrations although success is predicted. We compare their structure with the nearby successful cases of s25.4 (s2014 series, $(M_4\mu_4, \mu_4) \approx (0.150, 0.0820)$), and s25.2, s25.5 (both from the s2014 series), and s25.8 (s2002 series), all of which group around $(M_4\mu_4, \mu_4) \approx (0.143, 0.0783)$. The successfully exploding models all have similar entropy and density structures, namely fairly low entropies ($s \lesssim 3$) and therefore high densities up to 1.81–$1.82\,M_\odot$, where the entropy jumps to $s \gtrsim 6$. The high mass-accretion rate leads to an early arrival of the $s = 4$ interface at the shock (~ 300 ms after bounce) and high accretion luminosity. Together with the strong decline of the accretion rate afterwards this fosters the explosion. In contrast, the two models that blow up less easily have higher entropies and lower densities so that the $s = 4$ mass shells (at $\sim 1.8\,M_\odot$ in s15.0 and at $\sim 1.82\,M_\odot$ in the s15.3) arrive at the shock much later (at ~ 680 ms and ~ 830 ms post bounce, respectively), at which time accretion contributes less neutrino luminosity. Moreover, both models have a pronounced entropy ledge with a width of $\sim 0.05\,M_\odot$ (s15.0) and $\sim 0.08\,M_\odot$ (s15.3) before the entropy rises above $s \sim 5$. This ledge is much narrower than in the majority of non-exploding models, where it stretches across typically $0.3\,M_\odot$ or more. The continued, relatively high accretion rate prohibits shock expansion and explosion. This is obvious from the fact that model s15.0 with the less extended entropy ledge exhibits a
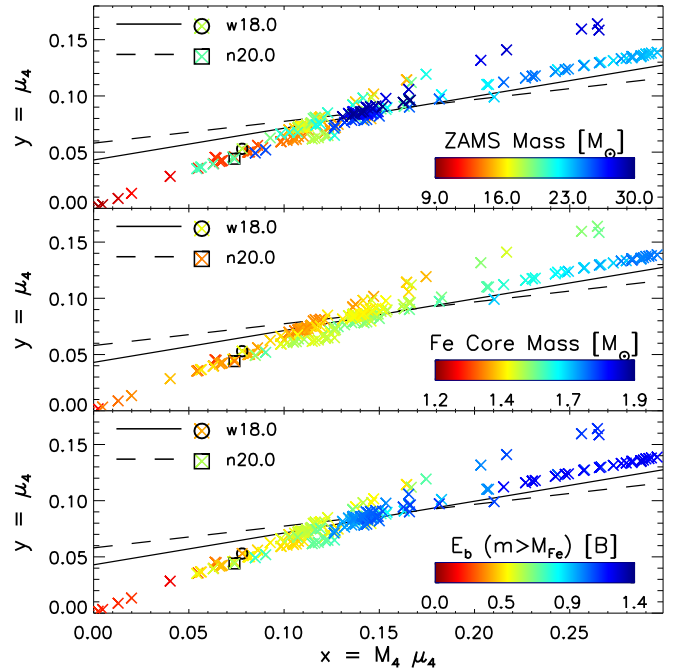
stronger tendency to explode and for some calibrations indeed does, whereas s15.3 with the wider ledge fails for all calibrations. Our diagnostic parameter μ_4 to measure the mass derivative in an interval of $\Delta m = 0.3\,M_\odot$, however, is dominated by the high-entropy level (low-density region) above the ledge and therefore underestimates the mass-accretion rate in the ledge domain, which is relevant for describing the explosion conditions. Again the abnormal structure of the s15.0 and s15.3 progenitors prevents our two-parameter classification from correctly describing the explosion behavior of these models.

3.5. Systematics of progenitor and explosion properties in the two-parameter plane

In Fig. 11 colored symbols show the positions of the progenitors of the s2014 series and those of the supplementary low-mass models with $M_{ZAMS} < 15\,M_\odot$ in the x-y-plane relative to the separation lines $y_{sep}(x)$ of exploding and non-exploding cases. In the upper panel the color coding corresponds to M_{ZAMS}, in the middle panel to the iron-core mass, M_{Fe}, and in the bottom panel to the binding energy of matter outside of the iron core. M_{Fe} is taken to be the value provided by the stellar progenitor model at the start of the collapse simulation in order to avoid misestimation associated with our simplified nuclear burning network and with inaccuracies from the initial mapping of the progenitor data. Since we use the pressure profile of the progenitor model instead of the temperature profile, slight differences of the derived temperatures can affect the temperature-sensitive shell burning and thus the growth of the iron-core mass.

While low-mass progenitors with small iron cores and low binding energies populate the region towards the lower left corner with significant distance to the separation curve, stars
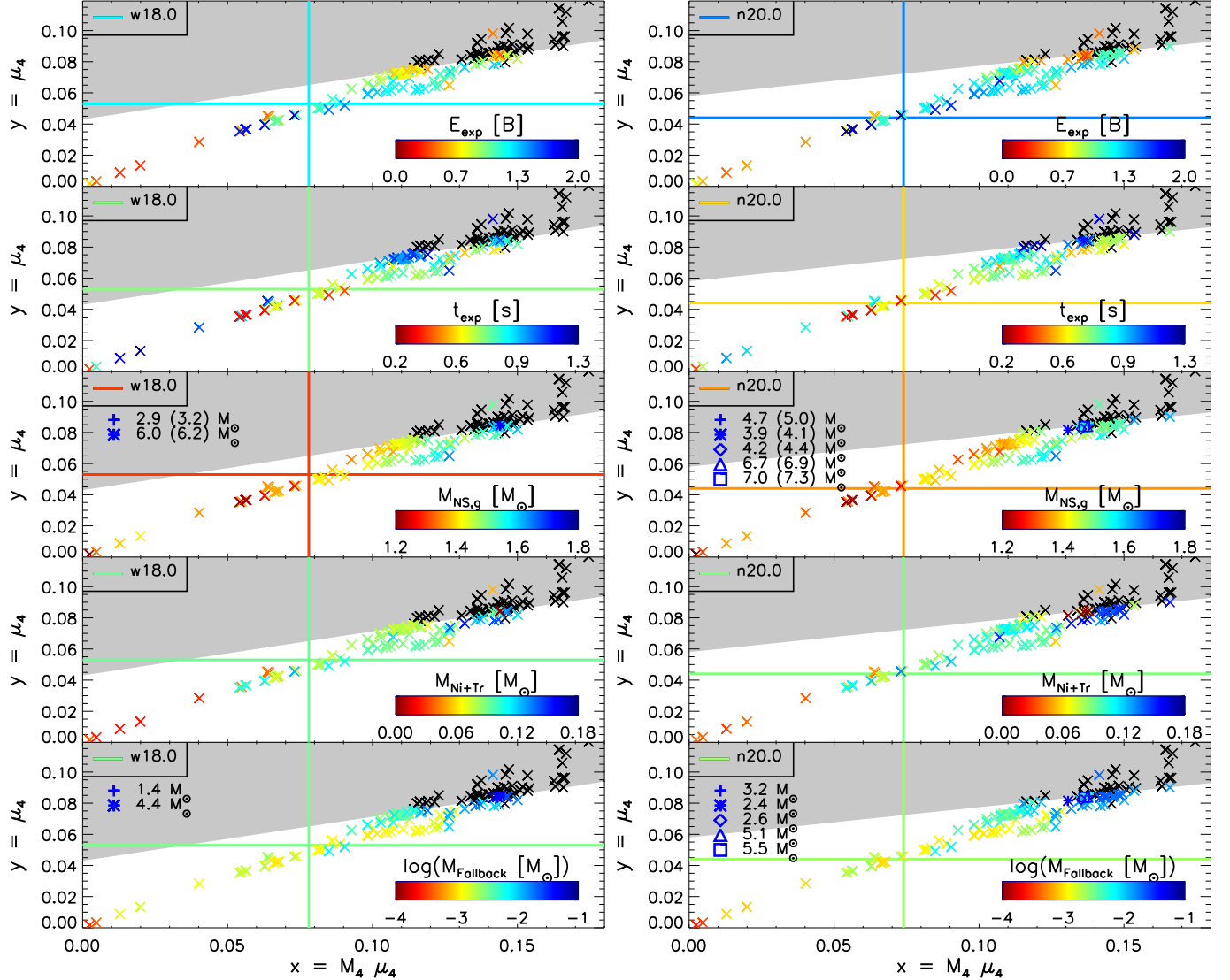
FIG. 12.— Explosion energies (1 B = 1 bethe = 10^{51} erg), post-bounce explosion times, gravitational neutron-star masses ($M_{\rm ns,g} = M_{\rm ns,b} - E_{\nu,\rm tot}/c^2$), ejected iron-group material (i.e., ^{56}Ni plus tracer masses), and fallback masses (*from top to bottom*) of the s2014 series and the supplementary low-mass progenitors with $M_{\rm ZAMS} < 15\,M_\odot$ for calibration models w18.0 (*left*) and n20.0 (*right*) in the *x-y* parameter plane. Black crosses correspond to BH formation cases, colored crosses to successful explosions. In the middle and bottom panels, the blue (partly overlapping) symbols correspond to fallback SNe with estimated BH masses (baryonic masses in parentheses) and fallback masses as listed in the legends. The horizonal and vertical lines mark the locations of the calibration models with the colors corresponding to the values of the displayed quantities.

above 20 $M_\odot$ with bigger iron cores and high binding energies can be mostly found well above the separation curve. However, there are quite a number of intermediate-mass progenitors above the line and higher-mass cases below. In particular, a lot of stars with masses between ~25 $M_\odot$ and 30 $M_\odot$ cluster around $y_{\rm sep}(x)$ in the $x \sim 0.13$–0.15 region. These stars are characterized by $M_{\rm Fe} \sim 1.4$–1.5 $M_\odot$ and high exterior binding energies. Some of them explode but most fail (cf. Fig. 9). The ones that group on the unsuccessful side are mostly cases with smaller iron cores, whose neutrino luminosity is insufficient to create enough power of neutrino heating to overcome the ram pressure of the massive infall.

Figure 12 displays the BH-formation cases of the s2014 series without associated SNe by black crosses in the *x-y*-plane. Successful SN explosions of this series plus additional $M_{\rm ZAMS} < 15\,M_\odot$ progenitors are shown by color-coded symbols, which represent, from top to bottom, the final explosion

energy ($E_{\rm exp}$, with the binding energy of the whole progenitor taken into account), the explosion time ($t_{\rm exp}$, measured by the time the outgoing shock reaches 500 km), the gravitational mass of the remnant (with fallback taken into account), the ejected mass of ^{56}Ni plus tracer element (see Sect. 2; fallback also taken into account), and the fallback mass. The left plot shows the results of our w18.0 calibration, the right plot for the n20.0 calibration. The gravitational mass of the NS remnant, $M_{\rm ns,g}$, is estimated from the baryonic mass, $M_{\rm ns,b}$, by subtracting the rest-mass equivalent of the total neutrino energy carried away in our simulations:

$$M_{\rm ns,g} = M_{\rm ns,b} - \frac{1}{c^2} E_{\nu,\rm tot} \,. \qquad (10)$$

Our estimates of NS binding energies, $E_{\rm ns,b} = E_{\nu,\rm tot}$, are roughly compatible with Lattimer & Yahil (1989) fit of $E_{\rm ns,b}^{\rm LY} = 1.5 \times 10^{53} (M_{\rm ns,g}/M_\odot)^2$ erg $= 0.084\,M_\odot c^2 (M_{\rm ns,g}/M_\odot)^2$. Blue

symbols in the middle and bottom panels mark fallback BH formation cases, for which gravitational and baryonic masses (the latter in parentheses) are listed in the panels. We ignore neutrino-energy losses during fallback accretion for both NS and BH-forming remnants.

Progenitors in Fig. 12 that lie very close to the separation line tend to produce weaker explosions that set in later than those of progenitors with a somewhat greater distance from the line. Moreover, there is a tendency of more massive NSs to be produced higher up along the x-y-band where the progenitors cluster, i.e., bigger NS masses are made at higher values of $x = M_4\mu_4$. Also the largest ejecta masses of ^{56}Ni and ^{56}Ni plus tracer are found towards the right side of the displayed progenitor band just below the boundary of the BH formation region.

Fallback masses tend to decrease towards the lower left corner of the x-y-plane in Fig. 12, far away from the separation curve, where predominantly low-mass progenitors are located, besides five progenitors around $20\,M_\odot$, which lie in this region because they have extremely low values of $E_b(m > M_4)$, see Fig. 9, and exceptionally small values of μ_4 (Fig. 11), and develop fast and strong explosions with small NS masses, large masses of ejected ^{56}Ni plus tracer, and very little fallback. Closer to the separation line the fallback masses are higher, but for successfully exploding models they exceed $\sim0.05\,M_\odot$ only in a few special cases of fallback SNe (cf. Fig. 3), where the fallback mass can amount up to several solar masses. We point out that the fallback masses in particular of stars below $\sim20\,M_\odot$ were massively overestimated by Ugliano et al. (2012). The reason was an erroneous interpretation of the outward reflection of reverse-shock accelerated matter as a numerical artifact connected to the use of the condition at the inner grid boundary. The reverse shock, which forms when the SN shock passes the He/H interface, travels backward through the ejecta and decelerates the outward moving matter to initially negative velocities. This inward flow of stellar material, however, is slowed down and reflected back outward by the large negative pressure gradient that builds up in the reverse-shock heated inner region. With this outward reflection, which is a true physical phenomenon and not a boundary artifact, the matter that ultimately can be accreted by the NS is diminished to typically between some $10^{-4}\,M_\odot$ and some $10^{-2}\,M_\odot$ of early fallback (see Fig. 3).

In a handful of high-mass s2014 progenitors (s27.2 and s27.3 for the w18.0 calibration and s27.4, s29.0, s29.1, s29.2, and s29.6 for the n20.0 set) the SN explosion is unable to unbind a large fraction of the star so that fallback of more than a solar mass of stellar matter is likely to push the NS beyond the BH formation limit. Such fallback SN cases cluster in the vicinity of $x \sim 0.13$–0.14 and $y \sim 0.080$–0.081 on the explosion side of the separation line. In the ZAMS-mass sequence they lie at interfaces between mass intervals of successfully exploding and non-exploding models, or they appear isolated in BH-formation regions of the ZAMS-mass space (see Figs. 4 and 9). Their fallback masses and estimated BH masses are listed in the corresponding panels of Fig. 12. Naturally, they stick out also by their extremely low ejecta masses of ^{56}Ni and tracer elements, late explosion times (around one second post bounce or later), and relatively low explosion energies (~0.3–0.5 B).

3.6. *Influence of the neutron star radius*

Basically, the accretion luminosity, which is given by $L_\nu^{\mathrm{acc}} \propto GM_{\mathrm{ns}}\dot{M}/R_{\mathrm{ns}}$, does not only depend on the PNS mass, M_{ns}, and the mass-accretion rate, $\dot{M}$, but also on the PNS radius, R_{ns}. One may wonder whether our two-parameter criterion is able to capture the essential physics although we disregard the radius dependence when using $x = M_4\mu_4$ as a proxy of the accretion luminosity.

For this reason, we tested a redefinition of $x = M_4\mu_4$ by including a factor $\langle R_{\mathrm{ns}}\rangle_{300\,\mathrm{ms}}^{-1}$, i.e., using $\tilde{x} \equiv M_4\mu_4\langle R_{\mathrm{ns}}\rangle_{300\,\mathrm{ms}}^{-1}$ instead[8]. Doing so, we found essentially no relevant effects on the location of the boundary curve. In fact, the separation of exploding and non-exploding models in the $\tilde{x}$-y-plane is even slightly improved compared to the x-y-plane, because $\langle R_{\mathrm{ns}}\rangle_{300\,\mathrm{ms}}^{-1}$ for most non-exploding models is larger than for the far majority of exploding ones. As a consequence, the non-exploding cases tend to be shifted to the left away from the boundary line, whereas most of the exploding cases are shifted to the right, also increasing their distances to the boundary line. This trend leads to a marginally clearer disentanglement of both model groups near the border between explosion and non-explosion regions. A subset of the (anyway few and marginal) outliers can thus move to the correct side, while very few cases can become new, marginal outliers. It might therefore even be possible to improve the success rate for the classification of explodability by a corresponding (minor) relocation of the boundary curve. The improvement, however, is not significant enough to justify the introduction of an additional parameter into our two-parameter criterion in the form of $\langle R_{\mathrm{ns}}\rangle_{300\,\mathrm{ms}}$, which has the disadvantage of not being based on progenitor properties and whose exact, case-dependent value cannot be predicted by simple arguments.

Because the line separating exploding and non-exploding models did not change in our test, the criterion advocated in this paper captures the basic physics, within the limitations of the modeling. While we report here this marginal sensitivity of our two-parameter criterion to the NS radius as a result of the present study, a finally conclusive assessment of this question would require to repeat our set of model calculations for different prescriptions of the time-dependent contraction of the inner boundary of our computational grid. The chosen functional behavior of this boundary movement with time determines how the proto-neutron star contraction proceeds during the crucial phase of shock revival. In order to avoid overly severe numerical time-step constraints, which can become a serious handicap for our long-time simulations with explicit neutrino transport over typically 20 seconds, we follow Ugliano et al. (2012) in using a relatively slow contraction of the inner grid boundary. It would be highly desirable to perform model calculations also for faster boundary contractions, which is our plan for future work. In view of this caveat the arguments and test results discussed in this section should still be taken with a grain of salt.

On grounds of the discussion of our results in the x-y-plane one can actually easily understand why the definition of the separation curve of exploding and non-exploding models in

---

[8] The radius R_{ns} of the proto-neutron star is defined by the radial position where the density is $10^{11}\,\mathrm{g\,cm}^{-3}$. As in panels d–f of Fig. 7, the time-averaging for $\langle R_{\mathrm{ns}}\rangle_{300\,\mathrm{ms}}^{-1}$ is performed from the passage of the $s = 4$ interface through the shock until the onset of the explosion for successful models and from the infall of the $s = 4$ interface until 300 ms later for non-exploding models. We also employ a normalization factor of 70 km to recover (roughly) the same range of values for $\tilde{x}$ as in the case of x.

the present paper did not require us to take into account a possible dependence of the accretion luminosity on the NS radius. Instead, we could safely ignore such a dependence when we coined our ansatz that $L_\nu \propto Mm'(r) \propto M_4\mu_4$. There are two reasons for that. On the one hand, the separation line in the $M_4\mu_4$-μ_4 plane is fairly flat. A variation of the NS radius corresponds to a horizontal shift of the location of data points in the x-y plane. However, with the contraction behavior of the neutron stars obtained in our simulations, only for (relatively few) points in the very close vicinity of the separation curve such a horizontal shift is sufficiently big to potentially have an influence on whether the models are classified as non-exploding or exploding. On the other hand, the models near the separation line typically blow up fairly late ($t_{exp} \gtrsim 0.6\,\mathrm{s}$), and the NS masses lie in a rather narrow range between roughly 1.4 $M_\odot$ and 1.6 $M_\odot$ for the gravitational mass (see Fig. 12). For such conditions the variation of the NS radius is of secondary importance (cf. Fig. 3 in Müller & Janka 2014). Low-mass progenitors with less massive NSs, whose radius (at the same time) can be somewhat larger (Fig. 3 in Müller & Janka 2014), however, are located towards the lower left corner of the x-y plane and therefore far away from the separation curve (compare Figs. 11 and 12). An incorrect horizontal placement of these cases (due to the omission of the dependence of the neutrino luminosity on the NS radius) does not have any relevance for the classification of these models.

3.7. *Brief comparison to previous works*

Our result of a complex pattern of NS and BH forming cases as function of progenitor mass was previously found by Ugliano et al. (2012), too, and was confirmed by Pejcha & Thompson (2015). Aside from differences in details depending on the use of different progenitor sets and different SN 1987A calibration models, the main differences of the results presented here compared to those of Ugliano et al. (2012) are lower explosion energies for progenitors with $M \lesssim 13\,M_\odot$ (see discussion in Sect. 2.3.4) and lower fallback masses as mentioned in Sect. 3.5. Based on simple arguments (which, however, cannot account for the complex dynamics of fallback), Pejcha & Thompson (2015) already expected (in particular for their parameterization (a)) that cases with significant fallback —in the sense that the remnant masses are significantly affected— should be rare for solar-metallicity progenitors. Our results confirm this expectation, although the ZAMS masses with significant fallback are different and less numerous than in the work by Pejcha & Thompson (2015). As pointed out by these authors, fallback has potentially important consequences for the remnant mass distribution, and the observed NS and BH masses seem to favor little fallback for the majority of SNe.

As discussed in detail by Ugliano et al. (2012), our explosion models (as well as parameterization (a) of Pejcha & Thompson 2015) predicts many more BH formation cases and more mass intervals of non-exploding stars than O'Connor & Ott (2011), who made the assumption that stars with compactness $\xi_{2.5} > 0.45$ do not explode. Roughly consistent with our results and those of Ugliano et al. (2012), Horiuchi et al. (2014) concluded on the basis of observational arguments (comparisons of the SN rate with the star formation rate; the red supergiant problem as a lack of Type-IIP SNe from progenitors above a mass of ~16 $M_\odot$) that stars with an "average" compactness of $\xi_{2.5} \sim 0.2$ should fail to produce canonical SNe (cf. Fig. 15 in Sukhbold et al. 2015).

A correlation of explosion energy and ^{56}Ni mass as found

by Pejcha & Thompson (2015) and Nakamura et al. (2015) (both, however, without rigorous determination of observable explosion energies at infinity) and as suggested by observations (see Pejcha & Thompson 2015 for details) is also predicted by our present results (but not by Ugliano et al. 2012 with their erroneous estimate of the fallback masses and the overestimated explosion energies of low-mass progenitors, see Sect. 2.3.4). Our models yield low explosion energies and low nickel production towards the low-mass side of the SN progenitors (see also Sukhbold et al. 2015). In contrast, the modeling approach by Pejcha & Thompson (2015) predicts a tendency of lower explosion energies and lower ^{56}Ni masses towards the high-mass side of the progenitor distribution (because of the larger binding energies of more massive stars), although there is a large mass-to-mass scatter in all results. This difference could be interesting for observational diagnostics. The modeling approach by Pejcha & Thompson (2015) seems to yield neutrino-driven winds that are considerably stronger, especially in cases of low-mass SN progenitors, than those obtained in the simulations of Ugliano et al. (2012) and, in particular, than those found in current, fully self-consistent SN and PNS cooling models, whose behavior we attempt to reproduce better by the Crab-motivated recalibration of the low-mass explosions used in the present work. Moreover, for the ^{56}Ni-E_{exp} correlation reported by Pejcha & Thompson (2015), a mass interval between ~14 $M_\odot$ and ~15 $M_\odot$ with very low explosion energies and very low Ni production, which does not exist in our models, also plays an important role. Nakamura et al. (2015) found a positive correlation of the explosion energy and the ^{56}Ni mass with compactness $\xi_{2.5}$. We can confirm this result for the nickel production but not for the explosion energy (cf. Sukhbold et al. 2015, Fig. 15 there). A possible reason for this discrepancy could be the consideration of "diagnostic" energies by Nakamura et al. (2015) at model dependent final times of their simulations instead of asymptotic explosion energies at infinity, whose determination requires seconds of calculation and the inclusion of the binding energy of the outer progenitor shells (see Fig. 3 and Sukhbold et al. 2015, Fig. 6, for the evolution of the energies in some exemplary simulations).

Since a comprehensive discussion of explosion energies, nickel production, and remnant masses is not in the focus of the present work, we refer the reader interested in these aspects to the follow-up paper by Sukhbold et al. (2015). For the same reason we also refrain here from more extended comparisons to the progenitor-dependent explosion and remnant predictions of other studies, in particular those of O'Connor & Ott (2011), Nakamura et al. (2015), and Pejcha & Thompson (2015). A detailed assessment of the different modeling methodologies and their underlying assumptions would be needed to understand and judge the reasons for differences of the results and to value their meaning in the context of supernova predictions based on the neutrino-driven mechanism. Such a goal reaches far beyond the scope of our paper.

4. CONCLUSIONS

We performed 1D simulations of SNe for a large set of 621 progenitors of different masses and metallicities, including the solar-metallicity s2002 series (Woosley et al. 2002) previously investigated by Ugliano et al. (2012) and the new s2014 models of Sukhbold & Woosley (2014) with their fine gridding of 0.1 $M_\odot$ in the ZAMS mass.

In order to obtain SN explosions in spherical symmetry, we adopt the methodology of Ugliano et al. (2012), using 1D hy-

drodynamics and approximate neutrino transport and a PNS-core neutrino source, but with improvements in a number of modeling aspects (e.g., a nuclear high-density EoS and a fully self-consistent implementation of nuclear burning through a small network, cf. Sect. 2.1). Explosions are triggered by a neutrino luminosity that is sufficiently large to overcome the critical threshold condition for shock runaway. This luminosity is fed by a progenitor-dependent accretion component during the post-bounce shock-stagnation phase as well as a component from the high-density core of the nascent NS. The core emission is also progenitor-dependent, because it scales with the mass of the hot accretion mantle that assembles around the cooler high-density core of the PNS during the pre-explosion evolution. The conditions for an explosion are thus tightly coupled to the progenitor structure, which determines the post-bounce accretion history.

Our approach contains a number of free parameters, whose values are calibrated by reproducing observational properties (explosion energy, ^{56}Ni mass, total neutrino energy and signal duration) of SN 1987A with suitable progenitor models of this SN. We consider five different such progenitors for our study, namely besides the s19.8 star of the s2002 model series of Woosley et al. (2002), which was used by Ugliano et al. (2012) as calibration model, also 15, 18, and 20 $M_\odot$ of Woosley and collaborators as well as a 20 $M_\odot$ model from Shigeyama & Nomoto (1990) (see Sect. 2.2).

Because 1D simulations cannot properly reproduce the period of continued accretion and simultaneous outflow that characterizes the early expansion of the revived shock in multi-dimensional simulations and delivers the explosion energy, our 1D models exhibit an extended episode of accretion that is followed by a strong early wind phase. The overestimated mass loss during the latter phase compensates for the enhanced preceding accretion, and the associated recombination energy yields the dominant contribution to the power supply of the beginning explosion. A detailed discussion of our methodology can be found in Sect. 2.3.

Overall, our results confirm the ZAMS-mass dependent explosion behavior that was found by Ugliano et al. (2012) for the s2002 model series. For the same explosion calibration this progenitor set and the newer s2014 models have basic features in common. Moreover, for all calibration cases we observe similar irregular patterns of successful explosions alternating with BH formation events above ∼15 $M_\odot$. The largest fraction of BH formation cases is obtained with the w20.0 calibration model, a 20 $M_\odot$ SN 1987A progenitor of Woosley et al. (1997), which explodes relatively easily and reproduces the SN 1987A ^{56}Ni yield with a fairly low ratio of explosion energy to ejecta mass of $E_{\rm exp}/M_{\rm ej} \sim 0.7$ only. The core neutrino source is correspondingly weak and enables successful SNe in a smaller subset of progenitors. On the other hand, we obtain the closest similarity of the explodability of the investigated progenitor sets when we use the s19.8 (Ugliano et al.'s) calibration model and Shigeyama & Nomoto (1990) n20.0 SN 1987A progenitor, which possess very similar compactness values $\xi_{2.5}$.

Non-exploding cases tend to correlate with *local* maxima of the compactness $\xi_{2.5}$, of the total binding energy outside of the iron core, $E_{\rm b}(m > M_{\rm Fe})$, and, most significantly, *local* maxima of the total binding energy $E_{\rm b}(m/M_\odot > M_4)$ outside of the mass coordinate $M_4 = m(s = 4)/M_\odot$, where the dimensionless entropy per nucleon reaches a value of 4. Many (but not all) non-exploding progenitors below ∼22 $M_\odot$ also coincide with local minima of $M_{\rm Fe}$ and, in particular, with minima of M_4. However, there are no fix threshold values of any of these characteristic parameters of the pre-collapse progenitor structure that could be used to discriminate favorable from non-favorable conditions for an explosion.

Guided by such insights we propose a two-parameter criterion to classify the explodability of progenitor stars by the neutrino-heating mechanism in dependence of the pre-collapse properties of these stars. The two structural parameters that turn out to yield the best separation of successful and unsuccessful cases are M_4 and the mass derivative $\mu_4 = {\rm d}m/{\rm d}r[M_\odot/(1000\,{\rm km})]^{-1}|_{s=4} = m'(s = 4)[M_\odot/(1000\,{\rm km})]^{-1}$ just outside of the $s = 4$ location, which we combine to a parameter $x \equiv M_4\mu_4$. The parameters x and $y \equiv \mu_4$ are tightly connected to the two crucial quantities that govern the physics of the neutrino-driven mechanism, namely the mass-accretion rate of the stalled shock, $\dot{M}$, and the neutrino luminosity L_ν. The former determines the ram pressure that damps shock expansion and can be mathematically linked to the mass derivative m' (see Eq. 5). The latter is a crucial ingredient for the neutrino heating that is responsible for shock revival and is dominated by the accretion luminosity and the PNS-mantle cooling emission during the crucial phase of shock revival. Both of these scale with $\dot{M}$ and/or the accretor mass (i.e., the PNS mass) so that $L_\nu \propto M_{\rm ns}\dot{M}$ expresses the leading dependence. Since the neutrino-driven explosions in our simulations set in shortly after the entropy interface and density jump around $s = 4$ have fallen through the shock (Fig. 2), M_4 can be taken as a good proxy of $M_{\rm ns}$ as the accretor mass, and μ_4 can serve as a measure for the mass accretion rate $\dot{M}$ of the PNS.

Higher values of M_4 tend to be favorable for an explosion as shown by Fig. 9, where many non-exploding cases (dark gray) correlate with local minima of M_4. The reason is that the neutrino luminosity scales (roughly) with $x = M_4\mu_4$ (the actual sensitivity of the neutrino-energy deposition to M_4 is even steeper). Therefore higher M_4 imply greater neutrino luminosities and stronger neutrino heating. In contrast, the influence of $y = \mu_4$ is ambivalent. On the one hand a high value of μ_4 increases the neutrino luminosity, on the other hand it also causes a large ram pressure that has to be overcome by neutrino heating. The effect of these competing influences is that a higher value of M_4 in association with a lower value of μ_4 favors explosions. Reversely, non-exploding cases in Fig. 9 are correlated with local minima of M_4 and maxima of μ_4. Visually, this means that explosion cases are preferentially located toward the lower right of the $M_4\mu_4$-μ_4 parameter space (cf. Figs. 6, 8, 12).

The parameters x and y therefore span a plane in which successful explosions and failures with BH formation are clearly separated. The progenitor stars populate an astonishingly narrow band that stretches from the lower left corner with the lightest stars to the upper right direction of the x-y-plane, where the massive progenitors with the biggest iron cores and highest binding energies of overlying material are located (see Fig. 11). While SNe can be found in the region of low values of y, i.e., for low mass-accretion rate, the non-exploding cases inhabit the domain of high y, but the limiting value of the mass-accretion rate that prevents the success of the neutrino-driven mechanism grows with the value of x. Both sectors in the x-y plane are separated by a boundary line that can be well represented by a linear function $y_{\rm sep}(x)$ (Eq. 9) with increasing slope. (The values of the dimensionless coefficients of this linear relation are listed for all calibration models in Ta-

ble 2.) Because of the physical meaning of the parameters x and y, there is a close correspondence between the separation line $y_{sep}(x)$ and the critical threshold luminosity $L_{\nu,crit}(\dot{M})$ that has to be exceeded to trigger runaway expansion of the accretion shock by neutrino heating. The rising slope of the separation curve in this context means that for each value of the neutrino luminosity, respectively x, there is an upper limit of the mass accretion rate, respectively y, up to which neutrino-driven explosions are possible, and that this BH-formation threshold value of y grows with x. The parameters x and y, computed from the progenitor profiles before collapse, allow one to judge whether a considered star is able to overcome the threshold neutrino luminosity for an explosion, or, in other words, whether its mass accretion rate stays below the critical limit above which the onset of the explosion is prevented.

Only ~1–3% of all investigated progenitors do not follow this discrimination scheme in their final fate but lie on the wrong side of the separation curve. These outliers are characterized by pathologies of their entropy and density profiles that describe the composition-shell structure in the Si-O-layers. Such special conditions lead to unusual combinations of mass accretion rate and PNS masses. Our two-parameter criterion expressed by the separation line $y_{crit}(x)$ therefore enables one, with a very high significance, to predict the explodability of progenitor stars via the neutrino-driven mechanism by referring to the properties of these stars as captured by the pair of parameters x and y.

Clausen et al. (2015) explore the interesting possibility that the death of massive stars in NS vs. BH formation may be better captured by a probabilistic description. The non-monotonic variations of explosion vs. non-explosion with ZAMS mass or compactness might be interpreted as stochasticity in the explosion behavior. However, by considering the problem in a more appropriate two-parameter space, our two-parameter criterion unmasks these putatively random variations as actually deterministic phenomenon. Clausen et al. (2015), in contrast, suggest a variety of factors besides ZAMS mass and metallicity, e.g. rotation, binarity, the strength of magnetic fields, stochastic differences in the pre-collapse structure or even in the explosion mechanism, that might introduce a randomness such that a star of given mass might not form either a NS or a BH but both with a certain probability. If such a diversity in the stellar destiny depends on a causal process, for example the presence of different amounts of spin, a deterministic description could still apply but would require an extension to a parameter space of more than the two dimensions combined by our current criterion, e.g., by adding extra dimension(s) that capture the role of rotation in the explosion mechanism. If, in contrast, truly stochastic effects like turbulent processes or chaotic fluctuations in the progenitor, decide about the stellar fate, a deterministic criterion for explodability would be ruled out and a probabilistic description would be indispensable.

Our study has a number of more caveats that need to be addressed. The understanding of the explosion mechanism(s) of massive stars is still incomplete, although considerable progress has been achieved in recent years due to the progress in 2D and 3D modeling and in particular also through improvements in the treatment of the crucial neutrino physics and transport in collapsing stellar cores (see, e.g., Janka et al. 2012; Janka 2012; Burrows 2013; Mezzacappa et al. 2015; Melson et al. 2015a,b; Lentz et al. 2015, and references therein). Without self-consistent 3D explosion simulations for large sets of progenitor stars being possible yet,

our study refers to a 1D modeling approach, in which not only the neutrino description is approximated in many aspects, but also the explosions have to be triggered artificially. We employ a boundary condition that replaces the high-density, low-entropy core of the nascent NS as a neutrino source, and we describe the time-dependent behavior of this core and of the coupling between the core and its hot accretion mantle by a simple, analytical model. Calibrating the involved free parameters by observational constraints from SN 1987A for the more massive stars and by comparison to results of sophisticated SN models for low-mass progenitors is intended to anchor our simplified description on empirical ground. Although the elements of this approximate approach appear qualified to capture the essence of the neutrino-heating mechanism in dependence of the progenitor-specific post-bounce accretion evolution (cf. Sect. 2.3 for details), confirmation by fully self-consistent, multi-dimensional SN calculations is ultimately indispensable. It is also evident that our study, which is only concerned with neutrino-driven explosions, cannot yield any information about the possibility and implications of other mechanisms to blow up stars, for example magnetorotational explosions of rapidly rotating stellar cores, which might be a consequence of magnetar or BH formation and could be associated with hypernovae and gamma-ray burst SNe (see, e.g., Mazzali et al. 2014) as well as ultra-luminous SNe (Woosley 2010; Kasen & Bildsten 2010; Sukhbold et al. 2015).

Our study employs pre-collapse models that emerge from 1D stellar evolution calculations of single, non-rotating SN progenitors with prescribed mass-loss histories. The results of our study naturally depend on the post-bounce accretion properties of the collapsing stars. The (iron and low-entropy) core masses as well as the entropy and density jumps at the composition-shell interfaces play an important role in setting the conditions for the neutrino-heating mechanism, which is obvious from the definition of our parameters x and y. It is conceivable that multi-dimensional hydrodynamics could lead to considerable changes of the stellar properties as functions of the progenitor mass (e.g., Arnett et al. 2015), and that asymmetries and perturbations in the shell-burning layers of the pre-collapse core might have important consequences for the development of SN explosions by the neutrino-driven mechanism (e.g., Arnett & Meakin 2011; Couch & Ott 2013, 2015; Müller & Janka 2015; Couch et al. 2015). We are hopeful that the basic insights of our study, in particular the existence of a two-parameter criterion for the explodability —expressed by a SN-BH separation line $y_{crit}(x)$ in the x-y-space and the tight connection between this curve and the critical luminosity condition $L_{\nu,crit}(\dot{M})$ of the neutrino-driven mechanism— possess more general validity. The explosion properties of the progenitor stars as functions of the ZAMS mass, however, do not only depend (moderately) on the considered SN 1987A progenitor models but will probably also change once multi-dimensional stellar evolution effects will be accounted for in the pre-supernova conditions.

REFERENCES

Arcones, A., Janka, H.-T., & L.Scheck. 2007, A&A, 467, 1227

Arcones, A., & Janka, H.-T. 2011, A&A, 526, AA160

Arnett, W. D., & Meakin, C. 2011, ApJ, 733, 78

Arnett, W. D., Meakin, C., Viallet, M., et al. 2015, arXiv:1503.00342

Bruenn, S. W. 1993, in Nuclear Physics in the Universe, ed. M. W. Guidry & M. R. Strayer (Bristol: IOP Publishing), 31

Bruenn, S. W., Lentz, E. J., Hix, W. R., et al. 2014, arXiv:1409.5779

Bruenn, S. W., Mezzacappa, A., Hix, W. R., et al. 2013, ApJ, 767, LL6

Buras, R., Rampp, M., Janka, H.-T., & Kifonidis, K. . 2006, A&A, 457, 281

Burrows, A. 2013, Reviews of Modern Physics, 85, 245

Burrows, A., & Goshy, J. 1993, ApJL, 416, L75

Clausen, D., Piro, A. L., & Ott, C. D. 2015, ApJ, 799, 190

Couch, S.M. 2013, ApJ, 775, 35

Couch, S.M. & O'Connor, E.P. 2014, ApJ, 785, 123

Couch, S. M., & Ott, C. D. 2013, ApJ, 778, LL7

Couch, S. M., & Ott, C. D. 2015, ApJ, 799, 5

Couch, S. M., Chatzopoulos, E., Arnett, W. D., & Timmes, F. X. 2015, arXiv:1503.02199

Dolence, J. C., Burrows, A., & Zhang, W. 2015, ApJ, 800, 10

Dolence, J. C., Burrows, A., Murphy, J. W., & Nordhaus, J. 2013, ApJ, 765, 110

Fernández, R. 2012, ApJ, 749, 142

Fischer, T., Whitehouse, S.C., Mezzacappa, A., Thielemann, F.-K., & Liebendörfer, M. 2010, A&A, 517, A80

Fryxell, B. A., Müller, E., & Arnett, W. D. 1989, MPA-Preprint 449 (Max-Planck Institut für Astrophysik, Garching)

Handy, T., Plewa, T., & Odrzywołek, A. 2014, ApJ, 783, 125

Hanke, F. 2014, PhD Thesis, Technische Unversität Munich

Hanke, F., Marek, A., Müller, B., & Janka, H.-T. 2012, ApJ, 755, 138

Hanke, F., Müller, B., Wongwathanarat, A., Marek, A., & Janka, H.-T. 2013, ApJ, 770, 66

Heger, A. 2003, private communication

Horiuchi, S., Beacom, J. F., Kochanek, C. S., Prieto, J. L., Stanek, K. Z., & Thompson, T. A. 2011, ApJ, 738, 154

Horiuchi, S., Nakamura, K., Takiwaki, T., Kotake, K., & Tanaka, M. 2014, MNRAS, 445, L99

Janka, H.-T. 2001, A&A, 368, 527

Janka, H.-T. 2012, Annual Review of Nuclear and Particle Science, 62, 407

Janka, H.-T., & Müller, E. 1996, A&A, 306, 167

Janka, H.-T., & Keil, W. 1998, in: Supernovae and Cosmology, eds. L. Labhardt, B. Binggeli, and R. Buser (Astronomisches Institut der Univ. Basel, Basel, 1998), p. 7; arXiv:astro-ph/9709012

Janka, H.-T., Kifonidis, K., & Rampp, M. 2001, in: Physics of Neutron Star Interiors, eds. D. Blaschke, N.K. Glendenning, and A. Sedrakian, LNP 578, 333; arXiv:astro-ph/0103015

Janka, H.-T., Hanke, F., Hüdepohl, L., Marek, A., Müller, B., & Obergaulinger, M. 2012, Progress of Theoretical and Experimental Physics, 2012, 010000

Janka, H.-T., Müller, B., Kitaura, F.S., & Buras, R. 2008, A&A, 485, 199

Kasen, D., & Bildsten, L. 2010, ApJ, 717, 245

Kifonidis, K. 2004, private communication

Kifonidis, K., Plewa, T., Janka, H.-T., & Müller, E. 2003, A&A, 408, 621

Kifonidis, K., Plewa, T., Scheck, L., Janka, H.-T., Müller, E. 2006, A&A, 453, 661

Kitaura, F.S., Janka, H.-T., & Hillebrandt, W. 2006, A&A, 450, 345

Lattimer, J. M., & Swesty, F. D. 1991, NuPhA, 535, 331

Lattimer, J. M., & Yahil, A. 1989, ApJ, 340, 426

Lentz, E.J., Bruenn, S.W., Hix, W.R., Mezzacappa, A., Messer, O.E.B., Endeve, E., Blondin, J.M., Harris, J.A., Marronetti, P., & Yakunin, K.N. 2015, ApJ, 807, L31

Liebendörfer, M. 2005, ApJ, 633, 1042

Marek, A. & Janka, H.-T. 2009,ApJ, 694, 664

Marek, A., Dimmelmeier, H., Janka, H.-T., Müller, E., & Buras, R. 2006, A&A, 445, 273

Mazzali, P. A., McFadyen, A. I., Woosley, S. E., Pian, E., & Tanaka, M. 2014, MNRAS, 443, 67

Melson, T., Janka, H.-T., & Marek, A. 2015a, ApJ, 801, L24

Melson, T., Janka, H.-T., Bollig, R., Hanke, F., Marek, A., & Müller, B. 2015b, ApJ, 808, L42

Mezzacappa, A., Bruenn, S.W., Lentz, E.J., Hix, W.R, Harris, J.A., Bronson, M.O.E., Endeve, E., Blondin, J.M., Marronetti, P., & Yakunin, K.N. 2015, eprint arXiv:1501.01688

Müller, B. 2013, private communication

Müller, B. 2015, MNRAS, 453, 287

Müller, B. & Janka, H.-T. 2014, ApJ, 788, 82

Müller, B., & Janka, H.-T. 2015, MNRAS, 448, 2141

Müller, B., Janka, H.-T., & Heger, A. 2012a, ApJ, 761, 72

Müller, B., Janka, H.-T., & Marek, A. 2012b, ApJ, 756, 84

Müller, B., Janka, H.-T., & Marek, A. 2013, ApJ, 766, 43

Müller, E. 1986, A&A, 162, 103

Murphy, J. W., & Burrows, A. 2008, ApJ, 688, 1159

Nakamura, K., Takiwaki, T., Kuroda, T., & Kotake, K. 2015, Publ. Astron. Soc. Japan, advance access

Nomoto, K., Sugimoto, D., Sparks, W. M., Fesen, R. A., Gull, T. R., & Miyaji, S. 1982, Nature, 299, 803

Nomoto, K., Tominaga, N., Umeda, H., Kobayashi, C., & Maeda, K. 2006, Nuclear Physics A, 777, 424

Nordhaus, J., Burrows, A., Almgren, A., & Bell, J. 2010, ApJ, 720, 694

O'Connor, E., & Ott, C. D. 2011, ApJ, 730, 70

Pejcha, O., & Thompson, T. A. 2012, ApJ, 746, 106

Pejcha, O. & Thompson, T. A. 2015, ApJ, 801, 90

Perego, A., Hempel, M., Fröhlich, C., et al. 2015, arXiv:1501.02845

Plewa, T., & Müller, E. 1999, A&A, 342, 179

Scheck, L., Janka, H.-T., Foglizzo, T., & Kifonidis, K. 2008, A&A, 477, 931

Scheck, L., Kifonidis, K., Janka, H.-T., & Müller, E. 2006, A&A, 457, 963

Scheck, L., Plewa, T., Janka, H.-T., Kifonidis, K., Müller, E. 2004, Physical Review Letters, 92, 011103

Shigeyama, T. & Nomoto, K. 1990, ApJ, 360, 242

Smartt, S., Eldridge, J. J., Crockett, R. M., & Maund, J. R. 2009, MNRAS, 395, 1409

Smith, N. 2013, MNRAS, 434, 102

Sukhbold, T., & Woosley, S. E. 2014, ApJ, 783, 10

Sukhbold, T., Ertl, T., Woosley, S. E., Brown, J. M., & Janka, H.-T. 2015, arXiv:1510.04643

Suwa, Y. 2012, IAUS, 279, 397

Suwa, Y., Yamada, S., Takiwaki, T., & Kotake, K. 2014, arXiv:1406.6414

Takiwaki, T., Kotake, K., & Suwa, Y. 2014, ApJ, 786, 83

Tominaga, N., Blinnikov, S. I., & Nomoto, K. 2013, ApJ, 771, L12

Tamborra, I., Hanke, F., Janka, H.-T., Müller, B., Raffelt, G.G., & Marek, A. 2014, ApJ, 792, 96

Thielemann, F.-K., Nomoto, K., & Hashimoto, M.-A. 1996, ApJ, 460, 408

Timmes, F. X., & Swesty, F. D. 2000, ApJS, 126, 501

Thompson, C. 2001, ApJ, 534, 915

Thompson, T. A., Quataert, E., & Burrows, A. 2005, ApJ, 620, 861

Ugliano, M., Janka, H.-T., Marek, A. & Arcones, A. 2012, ApJ, 757, 69

Utrobin, V. P. 2005, Astronomy Letters, 31, 806

Utrobin, V. P., & Chugai, N. N. 2011, A&A, 532, A100

Utrobin, V., Wongwathanarat, A., Janka, H.-Th. & Müller, E. 2014, arXiv:1412.4122

Wanajo, S., Janka, H.-Th., & Müller, B. 2011, ApJ, 726, L15

Woosley, S. E. 2007, private communication

Woosley, S. E. 2010, ApJ, 719, L204

Woosley, S. E., Heger, A., & Weaver, T. A. 2002, RevMPh, 74, 1015

Woosley, S. E., Heger, A., Weaver, T. A., & Langer, N. 1997, ArXiv Astrophysics e-prints [arXiv:astro-ph/9705146]

Woosley, S. E., Heger, A., Weaver, T. A., & Langer, N. 2007, private communication

Woosley, S. E., Pinto, P. A., & Ensman, L. 1988, ApJ, 324, 466

Yang, H., & Chevalier, R. A. 2015, ApJ, 806, 153